Effect of collagen degradation on the mechanical behavior and wrinkling of skin

Poorya Chavoshnejad,[1,*] Ali H. Foroughi,[1,*] Niranjana Dhandapani,[2] Guy K. German,[2,3] and Mir Jalil Razavi[1,†]
[1]*Department of Mechanical Engineering, Binghamton University, State University of New York, New York 13902, USA*
[2]*Department of Biomedical Engineering, Binghamton University, State University of New York, Binghamton, New York 13902, USA*
[3]*Department of Pharmaceutical Sciences, Binghamton University, State University of New York, Binghamton, New York 13902, USA*

(Received 22 January 2021; revised 12 July 2021; accepted 27 August 2021; published 10 September 2021)

Chronological skin aging is a complex process that is controlled by numerous intrinsic and extrinsic factors. One major factor is the gradual degradation of the dermal collagen fiber network. As a step toward understanding the mechanistic importance of dermal tissue in the process of aging, this study employs analytical and multiscale computational models to elucidate the effect of collagen fiber bundle disintegration on the mechanical properties and topography of skin. Here, human skin is modeled as a soft composite with an anisotropic dermal layer. The anisotropy of the tissue is governed by collagen fiber bundles with varying densities, average fiber alignments, and normalized alignment distributions. In all finite element models examined, collagen fiber bundle degradation results in progressive decreases in dermal and full-thickness composite stiffness. This reduction is more profound when collagen bundles align with the compression axis. Aged skin models with low collagen fiber bundle densities under compression exhibit notably smaller critical wrinkling strains and larger critical wavelengths than younger skin models, in agreement with *in vivo* wrinkling behavior with age. The propensity for skin wrinkling can be directly attributable to the degradation of collagen fiber bundles, a relationship that has previously been assumed but unsubstantiated. While linear-elastic analytical models fail to capture the postbuckling behavior in skin, nonlinear finite element models can predict the complex bifurcations of the compressed skin with different densities of collagen bundles.

DOI: 10.1103/PhysRevE.104.034406

I. INTRODUCTION

As the largest organ of the body, skin is a complex composite structure that acts as a mechanical, chemical, and microbial barrier to the environment, regulates temperature and water content of the body, and enables the sense of touch [1,2]. This composite tissue consists of three major layers; the epidermis, the dermis, and the hypodermis, or subcutaneous layer [3]. Each major layer has multiple sublayers with different compositions, structures, and mechanical properties. As a result, accurate studies of skin mechanics are nontrivial. For instance, the epidermis is the outer layer of the skin and is made up of four or five sublayers depending on its location on the body, all with varying mechanical properties. The outermost epidermal layer is the stratum corneum (SC), which acts as a barrier to the typically drier external environment and is notably stiffer than the other sublayers. The annotated histological tissue cross section in Fig. 1(a) shows the multilayered composite structure of human skin.

Below the most superficial stratum corneum and living viable epidermis tissue is the dermis, a dense layer of connective tissue comprised of collagen fiber bundles, elastin, fibroblasts, and extracellular ground substance. Collagen bundles are widely believed to be responsible for the strength and mechanical integrity of the skin and act as a compliant substrate supporting the epidermis [4]. The dermis is divided into two sublayers, a thin papillary layer above a thick reticular layer, respectively, composed of thin and thick collagen fiber bundles [5]. Beneath the dermis sits the hypodermis, a soft fatty layer primarily composed of adipose cells that connect the superficial skin to the bones and muscles. The thickness and mechanical properties of these layers are known to differ considerably and vary with age and anatomical site [6,7]. Table I shows the range of thickness and elastic moduli of the different layers of human skin from various references. The reported values are greatly dependent on whether the skin is assessed *in vivo* or *in vitro* and what methods are used [8–10].

A major drive by the cosmetics industry is antiaging, and the cosmetic prevention or alleviation of wrinkles [4,7,32]. Strategies include instant-active skin tensioning agents that temporarily pull out wrinkles through the application of a drying polymeric film on the skin, and methods to restore the skin dermis to a less-aged state, such as increased elasticity and collagen content to reduce the appearance of wrinkles [5,33–36]. The mechanistic cause of how those technologies work [37,38] and the fundamental cause of age-induced wrinkling itself [11,16,38,39] are unclear and are being examined. In general, however, skin aging is a complex biological process caused by intrinsic (chronological aging) as well as numerous extrinsic factors that include solar photoaging [4,40–45]. Chronological aging primarily affects the collagen of the papillary dermis, while photoaging primarily reduces the stability of collagen bundles in the reticular dermis [46]. Unprotected sun exposure and cigarette smoking are the major causes of extrinsic aging as they damage the connective tissue and change material properties in the dermal layer [34,35,40].

Contemporary experimental studies have shown connective tissue damage plays a vital role in the development of

*These authors contributed equally to this work.
†mrazavi@binghamton.edu

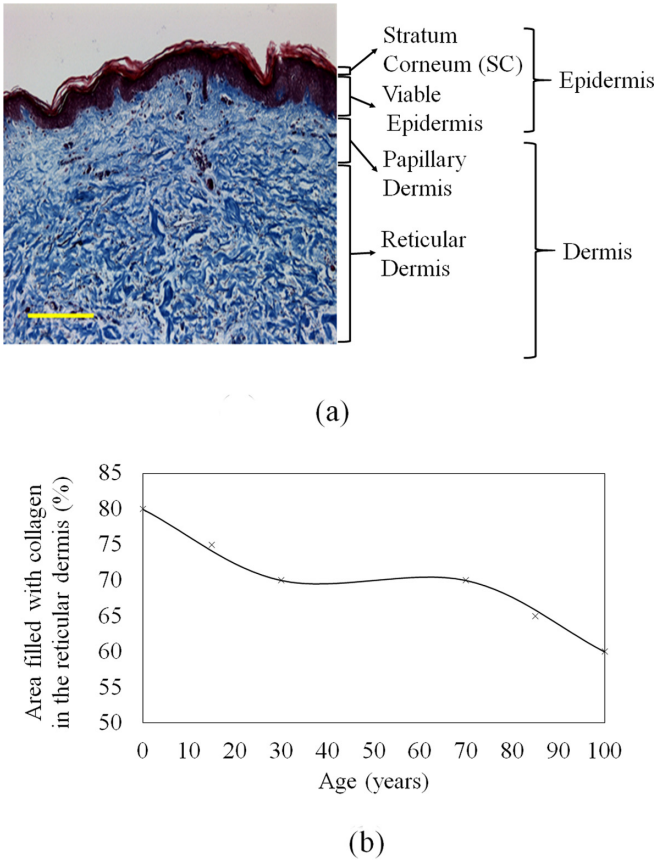

FIG. 1. Structural properties of heterogeneous and anisotropic human skin and their dependency on age. (a) Histological section of full-thickness human skin tissue annotated with the different skin layers. The hypodermis layer is not included. The scale bar denotes 200 μm. (b) The percentage of area occupied (AO) by collagen in the reticular dermis as a function of age. AO is representative of the density of collagen bundles and is characterized by quantifying the ratio of the area occupied by bundles to the total area of the matrix. Panel (b) has been modified from Ref. [5] and used with permission from Wiley.

wrinkles during aging [47]. Fragmentation and degradation of collagen fibers that decrease the overall density of collagen bundles has been reported as a result of aging [4,48–50]. Collagen type I makes up approximately 80% of dermal collagen fibers, and ∼70% of dry skin mass is composed of that type [4,51]. However, there is a remarkable reduction in collagen bundle density during aging, caused by degradation by solar UV absorption or matrix metalloproteinase (MMPs) activities [34,48,49,52]. Figure 1(b) elucidates this age-induced decrease in collagen bundle density. Dermal fiber bundle densities deteriorate monotonically by ∼1% per year [49]. The percentage of the area filled with collagen bundles reduces from 80% in newborn skin to 60% aged 100 years. Further, changes in average collagen bundle orientation vary with age [5]. While the orientation of collagen bundles is strongly aligned in newborn and aged skin, collagen bundles are disorganized in middle-aged skin [5]. Complicating a clear understanding of the mechanistic process of the aging process, new collagen synthesis reduces with age [53].

To date, it remains unclear how the degradation and fragmentation of collagen fiber bundles in the dermis alters the complex mechanical properties of skin that ultimately lead to visible signs of aging. While extensive experimental studies have revealed factors that are associated with aging, *in vivo* studies cannot distinguish the relative influence of the different tissue layer mechanical properties, and *ex vivo* studies cannot mimic *in vivo* conditions because of the inherent loss of skin tension upon excision. Moreover, there is a lack of sufficiently complex theoretical-computational frameworks that can adequately unravel the mechanism that causes age-based wrinkling. A majority of analytical and computational mechanical skin models have only studied the wrinkling mechanism when restricted to idealized conditions [11–15,54–57]. In those prior studies, the dermis is typically modeled as isotropic or a transversely isotropic layer to simplify the complex distributions and orientations of the collagen fiber bundles [58–61]. The prior research primarily examined the effect of geometry and mechanical properties of layers on the wrinkling patterns of compressed skin [11], rather than the aging process directly. As a step toward filling that gap, we model skin as a complex, composite tissue with an anisotropic dermal layer of collagen fiber bundles with distributed orientations in a soft matrix. The mechanistic process of aging is examined via the incremental elimination of collagen bundles. As a step toward better understanding the role of the relationship between collagen fiber bundles and the mechanistic process of aging and skin wrinkling, we employ a two-dimensional model to compare computational results with analytical results rather than utilizing a full-scale three-dimensional model.

II. METHODS

A. Experimental method

1. Tissue preparation and paraffin-based histology

Deidentified 62-year-old abdominal cadaveric human full-thickness skin was obtained from ConnectLife, NY. For our study, abdominal tissue was chosen because it is an anatomical site that typically experiences little ultraviolet radiation from the sun, which is known to induce collagen degradation

TABLE I. Reported thicknesses and material properties of skin layers from various references.

Layer	Thickness	Elastic modulus (MPa)	References
Stratum corneum (SC)	10–30 (μm)	0.6–100	[6,9,11–31]
Viable epidermis	30–100 (μm)	0.1–10	
Dermis	0.1–4 (mm)	0.03–0.2	
Hypodermis	1.1 (μm)–1.2 (mm)	0.05–0.1	

[62,63]. In accordance with the Department of Health and Human Services regulations, 45 CFR 46.101:b:4, an exempt approval (3002-13) was attained to perform research using deidentified tissue samples. Adipose tissue was excised from the dermis using a dermatome set to its maximum thickness capacity of 2.4 mm. A circular skin specimen of radius 6 mm is then excised with a biopsy punch. The tissue sample is fixed, sectioned, stained, and imaged, as previously reported [30], to obtain the histological image shown in Fig. 1(a).

2. Tissue cryosectioning and collagen fiber bundle orientation analysis

A rectangular specimen 10×15 mm in size is excised from the full-thickness skin specimen and chemically fixed overnight in 10% neutral buffered formalin solution (VWR, LLC, Radnor, PA). The sample is then immersed in a 30% weight/volume sucrose (sugar, crystals, Macron Chemicals, NJ, USA) solution in $1\times$ PBS (Amresco, OH, USA), until the tissues sink to the base of the container. The sunken tissue is placed inside a plastic mold containing Optimal Cutting Temperature (OCT) (TFM, General Data, OH, USA) medium, which is then snap frozen using liquid nitrogen. This embedded skin specimen is sectioned in the reticular dermal region using a cryostat (CryoStar NX50, Thermo Scientific, USA). The 14 μm thick cross sections are then laminated onto a glass slide. These cross sections are hydrated in de-ionized water for 30 s to dissolve the OCT medium, followed by immersion in Picrosirius stain (0.5 g of Direct Red 80, Sigma Aldrich, India, in 500 ml of 1.2% saturated aqueous solution of picric acid, RICCA, TX, USA) for 5 min, 1% aqueous acetic acid (Electron Microscopy Sciences, PA, USA) for 2 min to remove any excess stain, 100% ethanol (Koptec, DLI, PA, USA) for 2 min to dehydrate the tissue, and finally xylene (VWR, Histology Grade, PA, USA) for 2 min to clear the tissue. Sections are finally mounted onto glass cover slips using tissue mounting medium (Cytoseal 60, Thermo Scientific, MI, USA). Sample images are captured using a charge-coupled device (CCD) camera (Andor Clara, Belfast, Northern Ireland) mounted to a Nikon Eclipse Ti inverted microscope (Nikon, Melville, NY, USA) with a $10\times$ (Nikon Plan Fluor) objective lens when illuminated with a SOLA 6-LCR-SB (Lumencor light engine, Beaverton, OR, USA). Distributions of collagen fiber bundle orientation are quantified using the DIRECTIONALITY tool in IMAGEJ software, with a directionality histogram ranging between $\pm 90°$ in $2°$ bins. Figure 2 shows the arrangement, tortuosity, and density of collagen bundles in the papillary dermis of a 62-year-old abdominal skin specimen. The normal distribution of the collagen bundles will be used as the basis in the computational models, in agreement with prior studies [64,65].

B. Analytical method

While studies of wrinkling in multilayer systems date back half a century [66], recent studies have provided insight into the fundamental understanding of buckling instabilities and highlighted their relevance to numerous biomechanical phenomena [67–69], including wrinkle formation and growth during aging. In this study, we examine skin wrinkling under compressive loading using a composite model comprised

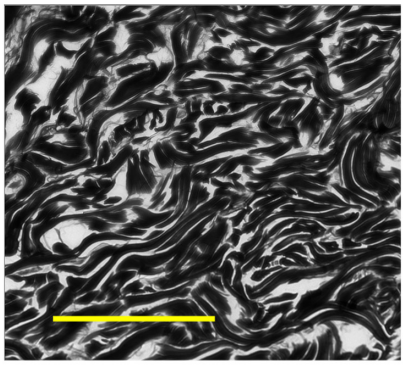

(a)

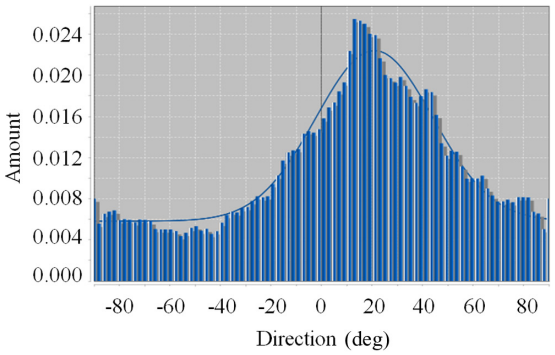

(b)

FIG. 2. Collagen distribution and orientation in a skin sample. (a) Horizontal transverse cross section of skin in the reticular dermal layer, parallel to the skin surface, displaying tortuous collagen fiber bundles. The scale bar denotes 200 μm. (b) Histogram of collagen fiber bundle directionality from panel (a) using the DIRECTIONALITY tool in FIJI [109–111]. (Blue curve) Least square best-fit Gaussian distribution (mean: 21.03°, standard deviation: 23.17°) to the histogram revealing normally distributed collagen orientations. An angle of 0° denotes alignment in panel (a) along the long axis of the scale bar with positive angles increasing in a counterclockwise direction.

of three layers: a stiff top layer representing the superficial stratum corneum (SC), a softer isotropic intermediate layer representing the viable epidermis (VE), and an anisotropic substrate representing the dermis (DE). Figure 3 provides a schematic representation of the model. The SC and VE are distinguished intentionally because of the notably larger elastic modulus of the SC. The hypodermis layer is excluded from the model as it is comparatively farther from superficial wrinkles.

In-plane compression of this three-layer structure can be studied analytically by modeling it as a beam lying on a foundation. A uniform compressive displacement is applied to the right boundary, while the left boundary is longitudinally fixed. The model base is frictionless and fixed laterally along the y axis. The free top boundary can freely deflect.

Dependent on the elastic modulus of the intermediate VE layer, two distinct wrinkling modes can occur: mode I: wrinkling of a composite beam (SC and VE combined) on a single layer DE substrate, and mode II: wrinkling of the stiff SC

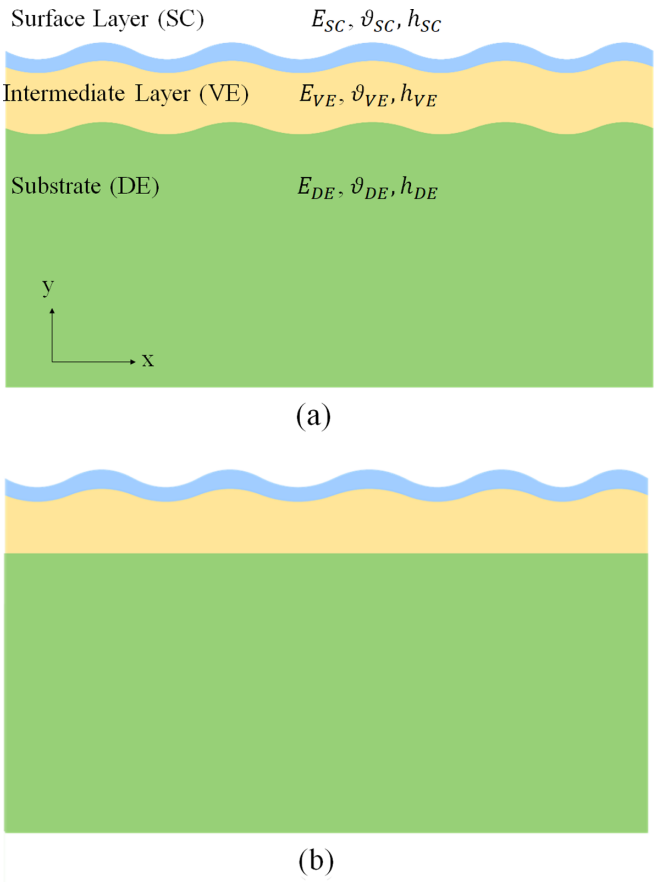

FIG. 3. Schematic of the three-layer skin model which consists of the stratum corneum (SC), viable epidermis layer (VE), and dermal layer (DE). E_{SC}, E_{VE}, E_{DE}, ϑ_{SC}, ϑ_{VE}, ϑ_{DE}, h_{SC}, h_{VE}, and h_{DE} are Young's modulus of SC, Young's modulus of VE, Young's modulus of DE, Poisson's ratio of SC, Poisson's ratio of VE, Poisson's ratio of DE, the thickness of SC, the thickness of VE, and the thickness of DE, respectively. (a) Mode I: wrinkling of a composite beam (SC and VE combined) on a single layer substrate (DE). (b) Mode II: wrinkling of the stiff top layer (SC) on a composite substrate (VE and DE combined).

top layer on a composite substrate (VE and DE combined) [68]. To solve this problem analytically, we first use the Euler-Bernoulli beam theory by neglecting shear effects [68]. Secondly, we assume a semi-infinite substrate. Finally, we consider all materials to be isotropic and linearly elastic. In this study the term "analytical method" refers to the analytical solution of the three-layer system described in the present section. In this analytical method, the values of Young's modulus of the substrate (E_{DE}) are obtained from the computational models presented in the next section.

Each wrinkling mode yields a different critical strain for the onset of wrinkling, established from the following equation:

$$\varepsilon_c = \min\left(\varepsilon_c^{\mathrm{I}}, \varepsilon_c^{\mathrm{II}}\right), \tag{1}$$

where ε_c is the critical wrinkling strain, and $\varepsilon_c^{\mathrm{I}}$ and $\varepsilon_c^{\mathrm{II}}$ are critical wrinkling strains calculated for mode I and II, respectively [70–73]. A MATLAB code was developed to solve for both modes and determine the active wrinkling mode.

To calculate the critical strain and critical wavelength for wrinkling in mode I, the stress equilibrium equation for a composite beam lying on an elastic foundation is

$$\bar{E}_b I \frac{d^4 w}{dx^4} + F \frac{d^2 w}{dx^2} + Kw = 0, \tag{2}$$

where w is the in-plane deflection of the composite beam along the y axis; I is the second moment of inertia of the composite beam; $I = \frac{(h_{\mathrm{SC}}+h_{\mathrm{VE}})^3}{12}$, and h_{SC} and h_{VE} are the thicknesses of the SC and VE layers, respectively; F is the external compressive force per unit length of the composite beam applied to the left and right side of the beam; and K is the stiffness of the substrate. The bending modulus of the composite beam, $\bar{E}_b$, is established from the following equation [68]:

$$\bar{E}_b = \frac{1 + m^2 n^4 + 2mn(2n^2 + 3n + 2)}{(n+1)^3(1+mn)} E_{\mathrm{sc}}^*, \tag{3}$$

where m and n depend on the material properties and geometry of the model, with

$$m = \frac{E_{\mathrm{VE}}^*}{E_{\mathrm{SC}}^*}, \quad n = \frac{h_{\mathrm{VE}}}{h_{\mathrm{SC}}}, \quad E_{\mathrm{SC}}^* = \frac{E_{\mathrm{SC}}}{\left(1-\upsilon_{\mathrm{SC}}^2\right)^2},$$
$$E_{\mathrm{VE}}^* = \frac{E_{\mathrm{VE}}}{\left(1-\upsilon_{\mathrm{VE}}^2\right)^2}. \tag{4}$$

Here, E_{SC} and E_{VE} are Young's moduli of the SC and VE layers, υ_{SC} and υ_{VE} are their respective Poisson's ratios, and E_{SC}^* and E_{VE}^* are their respective plane-strain moduli of elasticity.

Assuming the deflection of the beam, w, to be a cosine function of x,

$$w = W_0 \cos\left(\frac{2\pi x}{\lambda}\right), \tag{5}$$

where λ is the wrinkle wavelength, and W_0 is the wrinkle amplitude. Taking the interfacial shear stress to be negligible, the foundation stiffness, K, is determined by the wrinkle wavelength and the elastic material properties of the foundation as [74]

$$K = \frac{4(1-\upsilon_{\mathrm{DE}})^2 \pi E_{\mathrm{DE}}^*}{(3-4\upsilon_{\mathrm{DE}})\lambda}, \tag{6}$$

where $E_{\mathrm{DE}}^* = E_{\mathrm{DE}}/(1-\upsilon_{\mathrm{DE}}^2)$ is the plane-strain modulus of the substrate (DE), and υ_{DE} is the Poisson's ratio of the substrate. Considering the dermis layer to be incompressible ($\upsilon_{\mathrm{DE}} = 0.5$), Eq. (6) reduces to

$$K = \frac{\pi E_{\mathrm{DE}}^*}{\lambda}. \tag{7}$$

Substituting the K and w in the governing equilibrium Eq. (2), F can be written as

$$F = \bar{E}_b I \left(\frac{2\pi}{\lambda}\right)^2 + \frac{E_{\mathrm{DE}}^* \lambda}{4\pi}. \tag{8}$$

The critical compressive strain corresponds to the minimum force (F_c^{I}) to onset wrinkling. Therefore, the wavelength satisfying $\partial F/\partial\lambda = 0$ corresponds to the critical wavelength

(λ_c):

$$\lambda_c = 2\pi(h_{\mathrm{SC}} + h_{\mathrm{VE}})\left(\frac{\bar{E}_b}{3E^*_{\mathrm{DE}}}\right)^{\frac{1}{3}}. \tag{9}$$

This optimum value for the wavelength can be used to calculate the critical compressive strain for the onset of wrinkling in mode I. The compressive strain of the composite beam is defined as the ratio of the compressive stress, $\frac{F_c^{\mathrm{I}}}{h\times 1}$, to the compressive modulus of the beam, $\bar{E}_t$:

$$\varepsilon_c^{\mathrm{I}} = \frac{F_c^{\mathrm{I}}}{\bar{E}_t h} = \frac{1}{4}\frac{\bar{E}_b}{\bar{E}_t}\left(\frac{3E^*_{\mathrm{DE}}}{\bar{E}_b}\right)^{\frac{2}{3}}, \tag{10}$$

where $h = h_{\mathrm{SC}} + h_{\mathrm{VE}}$ and $\bar{E}_t$ is the equivalent compressive modulus of the composite beam and is calculated as

$$\bar{E}_t = E_{\mathrm{SC}}\frac{h_{\mathrm{SC}}}{h} + E_{\mathrm{VE}}\frac{h_{\mathrm{VE}}}{h}. \tag{11}$$

Please check the Appendix for the calculation of the critical strain and critical wavelength of mode II.

C. Computational method

The computational analysis is performed in two sections: linear buckling and nonlinear postbuckling. In the linear buckling section, all material properties of layers and collagen fibers are considered linear-elastic materials. With that assumption, the results of the analytical and computational methods are comparable. However, this assumption is valid only for small strains. In the nonlinear postbuckling section, there are large deformations in the models so all material properties are converted to their associated hyperelastic neo-Hookean materials.

1. Linear buckling

Developing a physiologically relevant multiscale computational model is achieved in two steps. First, the dermis is modeled as a single isolated layer to establish its equivalent elastic modulus for different collagen bundle densities and average fiber orientations. Here, we do not distinguish the papillary from the reticular dermis. In the first step, in a 10 × 2 mm rectangle model, the collagen bundles are modeled as embedded truss elements in a soft surrounding matrix using the embed constraint in ABAQUS finite element commercial software [75]. An embedded element method is used in this study to avoid extreme shear stress between stiff collagen bundles and the soft matrix under large strains as the result of the notable mismatch between their elastic moduli. An individual collagen bundle is modeled with multiple truss elements and the matrix is meshed using a four-node plane-strain element. Here, soft matrix refers to all constituents of the dermal layer except the collagen fibers. The embedded element method allows the finite element model of the collagen bundles to be directly incorporated into the mesh of the matrix without preprocessing complications. The embedded element method has been developed for composite materials with large deformations where the fibers and matrix are discretized separately and then assembled with specific constraints [76–79]. The embedded element method is used to reduce the convergence problem in the matrix-fiber shared nodes [80]. In this method, unlike other methods such as direct partitioning, each node of the fiber is connected to all nodes of the associated matrix's element. This method has several advantages over the direct method, such as avoiding high shear stresses between collagen bundles and the matrix, providing direct computation of bundles' strains, easily tracing the history of individual bundles, and reducing the computational cost. There is no interaction between crossing fibers at their intersecting points. However, the effect of interfiber interaction on the mechanical behavior of the bulk tissue is an interesting topic for further investigation [81,82]. A two-dimensional (2D) plane-strain element (CPE4R) is used to mesh all three layers. As wrinkling occurs in the model, a very fine mesh is needed at the top layer to eliminate the effect of mesh size in the model. After the mesh convergence process, the optimum mesh size is determined to be 4 μm at the SC layer. The density of collagen bundles is characterized by quantifying the ratio of the area occupied (AO) by bundles to the total area of the matrix. Therefore, AO is a parameter that represents the density of the bundles. Individual collagen bundles distributed in the dermis have elastic material of $E_C = 68$ MPa equal to the average reported Young's modulus for skin collagen fibers, and a diameter of 8 μm equal to the average collagen fiber bundle diameter [5,12]. The elastic modulus of the ground substance is set to 8.5 kPa, equal to the average of the reported range [12]. Bundle lengths vary randomly between 1 and 2 mm [5]. For simplicity, all collagen fiber bundles are taut and recruited in an unstressed state, rather than their tortuous *in vivo* configuration. For each collagen density, the model is subjected to a compression load, and the composite dermal elastic modulus is extracted from the recorded stress-strain curve. All analyses in this section are performed by the static general analysis in ABAQUS. To model age-induced collagen degradation, changes in the composite elastic modulus of the dermis are established for collagen densities declining from 80% AO to 50% AO [Fig. 1(b)], in 5% increments. As detailed in Fig. 4, this characterization is completed for models with six different collagen bundle arrangements: normally distributed bundles with average orientations (a) parallel with the uniaxial loading axis, (b) at 15°, (c) at 30°, (d) at 45°, (e) at 60° to the uniaxial loading axis, and (f) a random orientation of collagen fiber bundles. A normal distribution is used to distribute collagen bundle directions in agreement with the experimental evaluation in Fig. 2(b). However, we do recognize that other distributions of collagen bundle orientation have been reported [58]. A fixed standard deviation is set for all orientations as 23.17 equal to the obtained value from the experimental result. Figure 4(g) shows the collagen fiber configuration of an 80% AO dermal model with random distribution of orientations.

The second modeling step is to integrate the dermal model into a three-layer finite element composite skin model, as depicted in Fig. 3, to perform a linear buckling analysis. From this, changes in buckling with the different dermal layer mechanical properties are quantified. As detailed in Table I, the thicknesses of individual layers are held constant, with $h_{\mathrm{SC}} = 15$ μm, $h_{\mathrm{VE}} = 65$ μm, and $h_{\mathrm{DE}} = 2$ mm. While we recognize that the thickness of the layers varies during aging [5,47]; this aspect is not considered in this study. Moreover, while several models for the material behavior of the different skin

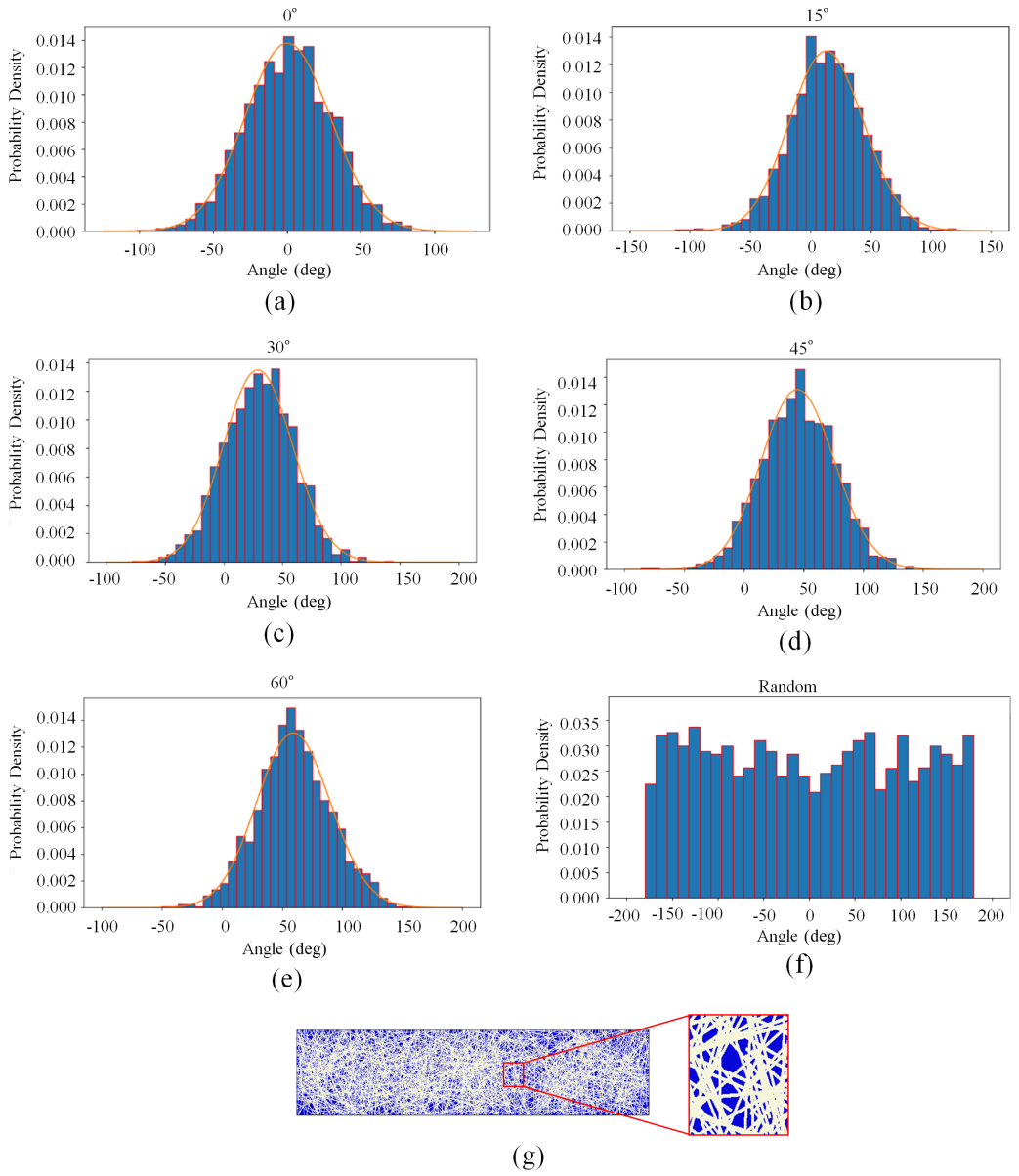

FIG. 4. Probability density of bundles' angles for models with distributions that are (a) horizontal, (b) 15°, (c) 30°, (d) 45°, (e) 60°, and (f) random. A 2D finite element model (g) of the dermal layer with randomly distributed collagen bundles at random angles. The layer is filled with 80% collagen bundles (AO = 80%). Blue depicts the soft matrix. The collagen bundles have not been rendered to the actual diameter to make visualization easier.

layers exist [8], in this section we assume that all layers of the skin model are linear and elastic. This assumption allows us to link analytical and computational models and compare their results. In this matter, the elastic modulus for SC and VE are assigned as $E_{SC} = 20$ MPa [29], and $E_{VE} = 5$ MPa, respectively. Except for the elastic modulus of the SC layer, the elastic moduli and thicknesses of each layer are selected equal to the average value of the reported range in Table I. A very large elastic modulus of the SC layer corresponds to the dehydrated skin [83,84]. Therefore, the elastic modulus of the SC layer is selected equal to 20 MPa to represent the normal skin.

2. Nonlinear postbuckling

In this section, the dynamic implicit method is used to study the effect of collagen degradation on the mechanical properties of the skin under large deformations. A 2D multilayer model as depicted in Fig. 5 is developed for the collagen bundles' orientations and densities. In contrast to the linear buckling, the whole analysis is performed in one step because the dermal layer includes collagen bundles. The material properties of collagen bundles, SC layer, viable epidermis, and ground substance are converted to neo-Hookean hyperelastic material models and their shear moduli are set to 11.41 MPa, 3.35 MPa, 0.84 MPa, and 1.4 kPa, respectively. To be compatible with the linear buckling section, the shear modulus of each layer is calculated using the linear relation between shear modulus and elastic modulus and considering Poisson's ratio equal to 0.5. The thickness of each layer and the diameter of the collagen bundles are identical to the linear buckling section and the collagen bundles are embedded in the ground

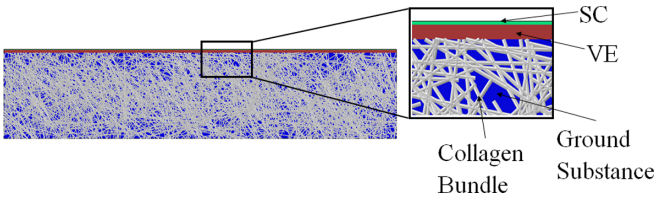

FIG. 5. A 2D dynamic finite element model of the skin with randomly distributed collagen bundles at random angles. The dermal layer is filled with 80% collagen bundles. Blue, gray, red, and green depict the ground substance, collagen bundles, viable epidermis, and SC, respectively. The collagen bundles have not been rendered to the actual diameter to make visualization easier.

substance. For each orientation of collagen fibers (0°, 15°, 45°, 60°, and random) two cases with 80% AO and 50% AO of collagen bundles are studied. Figure 5 shows a model with the 80% AO and random distribution in the orientation of the collagen bundles.

Each case is subjected to a 30% compressive strain. The amplitude (roughness) of wrinkles is measured by the roughness average (R_a) and root mean square (R_q) parameters using the following equations:

$$R_a = \frac{1}{l_r}\int_0^{l_r} |z(x)|\, dx, \tag{12}$$

$$R_q = \sqrt{\frac{1}{l_r}\int_0^{l_r} z^2(x) dx}, \tag{13}$$

where l_r is the projected length along the horizontal x axis of the system after deformation, and $z(x)$ is the equation of the deformed profile.

III. RESULTS AND DISCUSSIONS

A. Effect of collagen degradation on the mechanical behavior of dermis

Full-thickness human skin is compositionally and mechanically heterogeneous because of the fibrous structure of the dermal layer. This heterogeneity is revealed in Fig. 6(a), which shows the stress distribution in a dermal layer model exhibiting an 80% AO compressed with 10% strain. AO is the ratio of the area occupied by collagen bundles to the total area of the matrix. Here, the average collagen alignment is parallel with the axis of compression loading. Figure 6(b) shows an equivalent stress distribution after a reduction of collagen fiber density by 37.5%. Figures 6(c) and 6(d), respectively, show equivalent stress distribution to those in Figs. 6(a) and 6(b); however, here the collagen fibers are averagely oriented at 60° from the horizontal line. Stress distribution in the models shows that bundles with orientations closest to the compression direction experience the larger compressive stresses and support more of the load. This aligns with *in vivo* behavior, where the average orientation of the collagen fibers in those models is associated with the orientation of maximum skin tension. Patterns of maximum tension orientation are simply characterized by Langer's lines [85] in human skin; however recent studies have revealed subject-to-subject variations in orientation at identical anatomical sites [61]. Understanding the orientation of maximum skin tension is important to the cosmetics industry, dermatology, and surgery. Age-induced wrinkles typically align parallel with collagen fiber

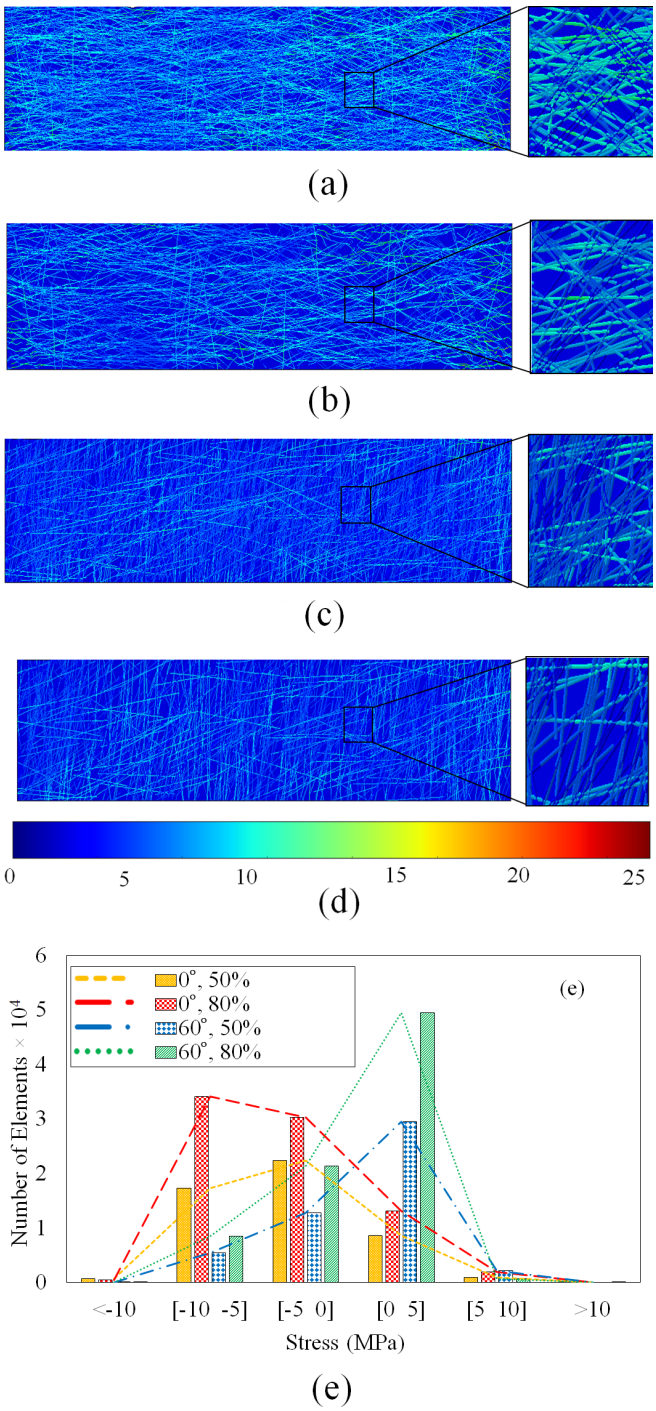

FIG. 6. Von Mises stress distribution (MPa) within a dermal tissue model subjected to a strain of $\varepsilon = 0.1$. Dermal tissue models exhibit (a) 80% and (b) 50% AOs for average collagen orientation aligned with the loading axis and (c) 80% and (d) 50% collagen fiber densities with 60° distributions of collagen orientations. (e) Axial stress distribution in the collagen fibers for the cases with 0° and 60° orientations in two different collagen densities under $\varepsilon = 0.1$ compressive strain.

orientations while incisions made across collagen fibers can lead to a greater risk of keloid scar formation [86].

Figure 6(e) shows the histogram graph of the stress distribution in the collagen bundles for the 0° and 60° cases with 80% and 50% AOs. For both cases, the number of collagen fibers that experience greater stresses is greater when the dermal layer is 80% collagen. In the cases with 80% AO, a greater number of fibers bear loads. For the same strain, the greater density collagen model experiences larger stresses than the reduced collagen density model. Furthermore, the results indicate that most of the collagen bundles in the 0° case are in compression, while for the 60° case most of the collagen bundles are in tension. The reason is that in the 0° case, collagen bundles resist against horizontal compression, while in the 60° case, collagen bundles are under tension to resist against the transverse expansion of the matrix because of the Poisson's ratio effect. Figure 6(e) indicates that the reduction of the collagen density in the dermal layer decreases the load-bearing capacity of the dermal layer.

Figure S1 in the Supplemental Material [87] shows the dependency of the elastic modulus of the dermal layer to the collagen densities and their orientations in the dermal layer. Results are presented for the cases with 0° orientation and 60° orientation of collagen bundles. The reduction in the density of collagen fibers reduces the elastic modulus of the dermal layer. When the collagen density decreases from 80% AO to 50% AO, the elastic modulus of the dermal layer decreases 35.98% and 25.44% for 0° and 60° distributions of collagen fibers, respectively. The dependency of the elastic modulus of the dermal layer to all of the densities and orientations is summarized in Fig. 7(a). Figures 7(a) and 7(b), respectively, show the effect of age-induced changes in average collagen fiber bundle density and average fiber orientation relative to the loading axis on the dermal elastic modulus. Dermal elastic moduli are extracted from stress vs strain slopes provided in Supplemental Fig. S1 [87] and other orientations (30°, 45°, and 60°) that have not been shown for ease of viewing. In Fig. S1, for each collagen density represented by AO, the model is subjected to a compression load, and the composite dermal elastic modulus is extracted from the recorded stress-strain curve; see the Methods section. The age-based degradation of collagen bundle density, established from Fig. 1(b), is employed to correlate elastic moduli with age effects in Fig. 7(b). Relative to randomly oriented fibers, dermal models with an average fiber orientation aligned along with the compression axis exhibit a greater elastic modulus for equivalent fiber bundle densities in Fig. 7(a). The elastic modulus further decreases when tensile loads are applied at increasingly more oblique angles to the average collagen fiber orientation, in agreement with the anisotropic mechanical behavior of skin established from *in vivo* and *ex vivo* experimental studies [59,61]. Moreover, decreases in collagen fiber density that occur with aging decrease the elastic modulus of the tissue layer, as shown in Fig. 7(b). The sensitivity of the dermal elastic modulus to the orientation of bundles is small for angles between 0° and 15°, in comparison with larger angles. This highlights the fact that degradation of fibers more aligned with the skin tension axis will play a comparatively larger role in the mechanical softening of the dermis, and the aging process. Aging for a century resulted in a 20% decrease of AO [5], which results in dermal softening by a maximum of 23.04%.

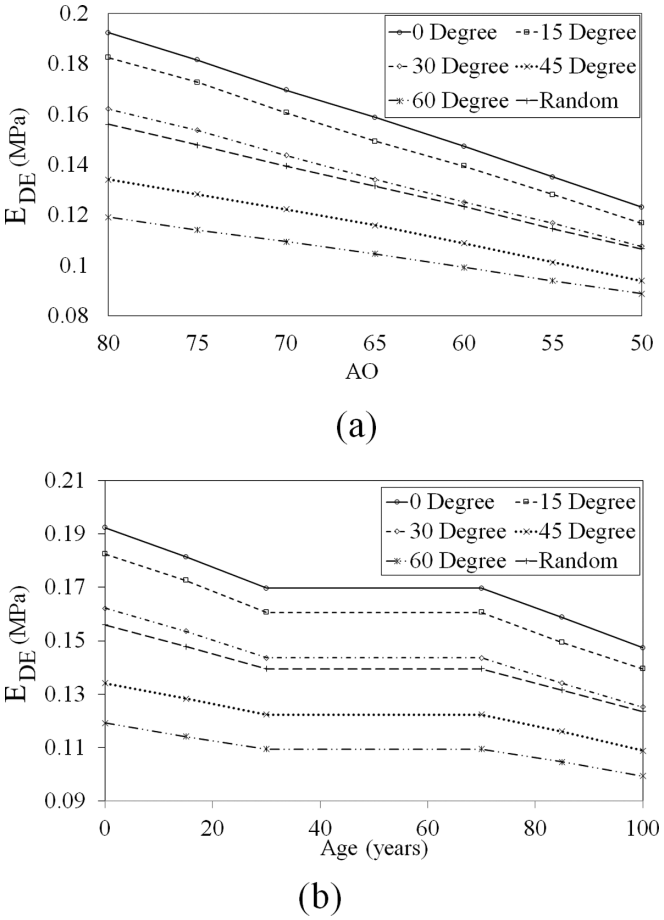

FIG. 7. (a) Variation of equivalent elastic modulus of the dermal layer during the aging process according to the different orientations of collagen bundles. (b) Variation of equivalent elastic modulus of the dermal layer by the decrease in AO by aging. AO is the ratio of the area occupied by bundles to the total area of the matrix.

B. Dependency of the wrinkling mode to the elastic modulus of the dermal layer

With a clear understanding of how collagen fiber degradation alters the mechanical properties of the dermis, the effect of aging on composite skin wrinkling can now be investigated. Figure 8 shows the critical strains of the two wrinkling modes for different E_{SC} and E_{VE} values from Table I. The two thickness values, h_{SC} and h_{VE}, are assumed to be the mean values of the ranges mentioned in Table I ($h_{SC} = 20\,\mu$m, $h_{VE} = 65\,\mu$m). Based on Eq. (1), for a certain set of (E_{VE}, E_{SC}) in Figs. 8(a), 8(c), and 8(e), the active wrinkling mode is either mode I or mode II, whichever is lower. Figures 8(b), 8(d), and 8(f) demonstrate the active wrinkling modes in the variable space (E_{VE}, E_{SC}). The boundary between the two regions of the wrinkling mode plots is staggered because the computation was performed for a discrete sets of variables (E_{VE}, E_{SC}). The critical strain graphs are plotted for three different values of Young's modulus of the substrate: minimum [$E_{DE} = 0.030$ (MPa)], mean [$E_{DE} = 0.115$ (MPa)],

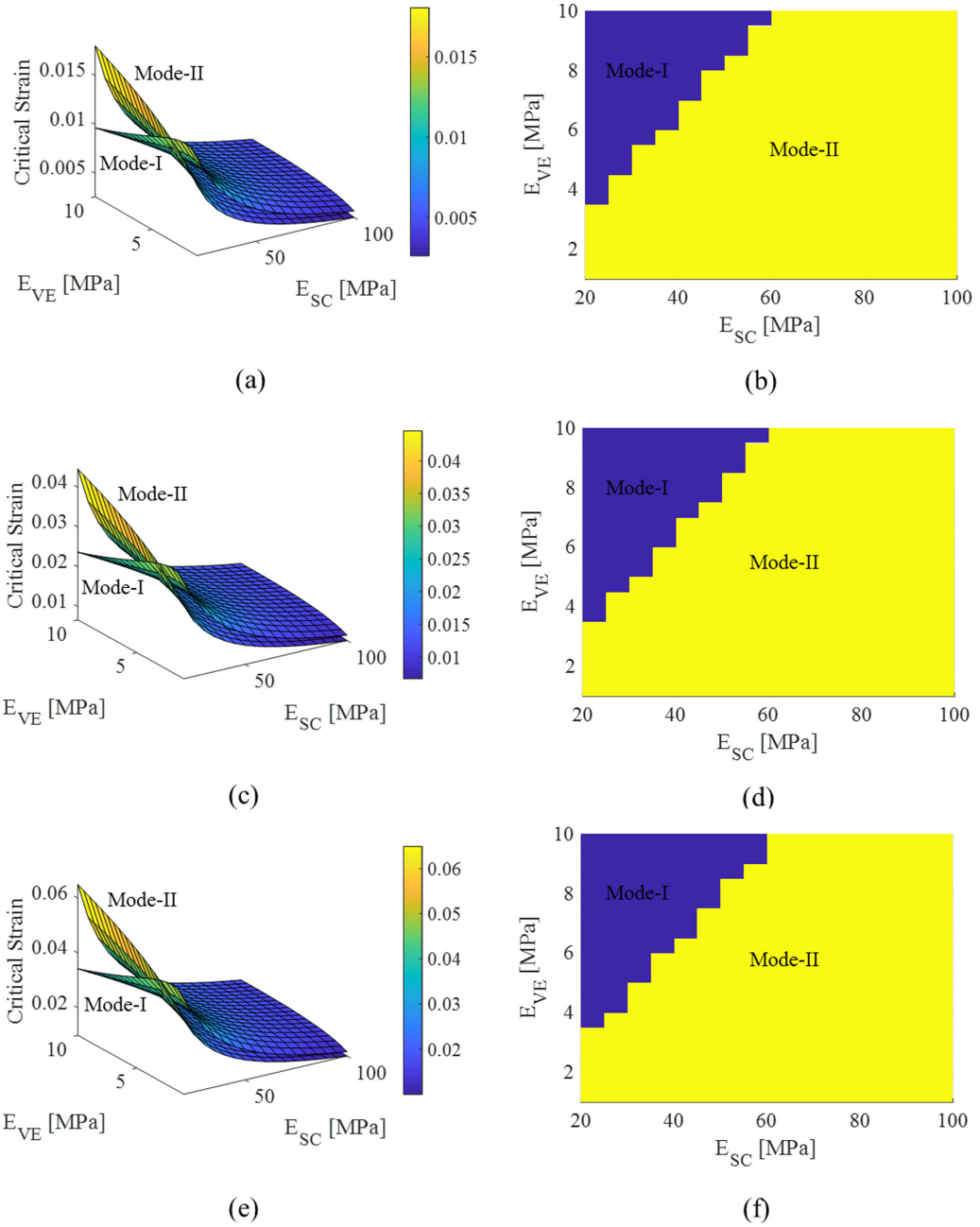

FIG. 8. The critical strains of the two wrinkling modes for different E_{SC} and E_{VE} values. (a), (c), (e) are the critical strain curves for both of the wrinkling modes, and (b), (d), (f) are the wrinkling mode region plots. The values of the Young's modulus of the substrate for (a), (c), and (e) are 0.030 (MPa), 0.115 (MPa), and 0.200 (MPa), respectively. Plots (b), (d), and (f) are the corresponding mode regions of (a), (c), and (e), respectively.

and maximum [$E_{DE} = 0.200$ (MPa)] values, based on the range specified in Table I. As shown in Fig. 8, regardless of the wrinkling mode, a stiffer SC layer results in a lower critical strain. That suggests the elevated stiffness of the outermost layer of the skin caused by dehydration or photoaging [83,88] facilitates the onset of wrinkling. This reduction in the critical wrinkling strain of skins with a greater SC's stiffness is consistent with the work of Kuwazuru *et al.* [88]. Furthermore, as demonstrated in Figs. 8(b), 8(d), and 8(f), a greater E_{SC} contributes to the transition from wrinkling mode I to mode II. If the SC is stiffer than a certain value, it tends to wrinkle alone on a composite substrate composed of VE and DE (mode II). Conversely, when the SC is not stiff enough, it is more likely that the two top layers wrinkle together on the DE layer as a substrate (mode I).

The stiffness of the VE layer is another parameter affecting the wrinkle mode transformation. As shown in Fig. 8, a stiffer VE layer results in a transition from mode II to mode I. As such, when the intermediate layer, VE, is stiff, it tends to wrinkle together with the superficial layer, SC. However, when the VE layer is not stiff enough, it is more likely to function as a substrate in combination with the DE layer, while the SC layer would wrinkle solely on top of this composite substrate. In addition to the stiffness of the top two layers of the skin

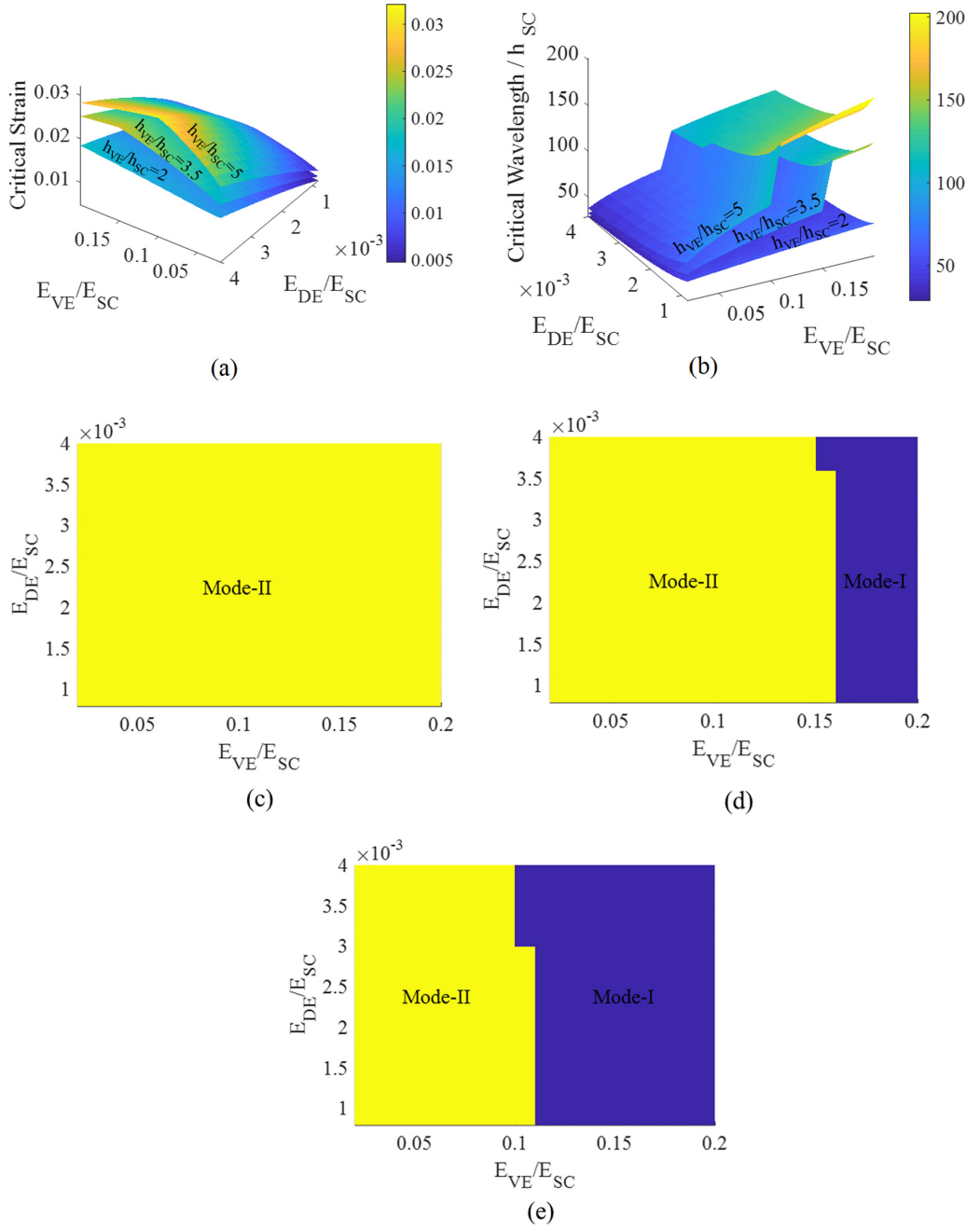

FIG. 9. (a), Variation of critical wrinkling strain with h_{VE}/h_{SC}, E_{VE}/E_{SC}, E_{DE}/E_{SC}; (b) variation of normalized critical wavelength (λ_c/h_{SC}) with h_{VE}/h_{SC}, E_{VE}/E_{SC}, E_{DE}/E_{SC}. Wrinkling mode region plots for (c) $h_{VE}/h_{SC} = 2$, (d) $h_{VE}/h_{SC} = 3.5$, and (e) $h_{VE}/h_{SC} = 5$.

(SC and VE), the elastic modulus of the DE layer influences the wrinkling onset. As shown in Figs. 8(a), 8(c), and 8(e), an increase in the stiffness of the substrate, E_{DE}, results in greater values of the critical wrinkling strain. Although E_{DE} influences the wrinkling onset by affecting the critical strain, it has almost no effect on the instability mode transformation. As demonstrated in Figs. 8(b), 8(d), and 8(f), an increase in E_{DE} does not affect the wrinkling mode region diagrams.

Figures 9(a) and 9(b) show the variation of critical strain (ε_c) and normalized critical wavelength (λ_c/h_{SC}) with three dimensionless ratios, namely, h_{VE}/h_{SC}, E_{VE}/E_{SC}, and E_{DE}/E_{SC}. Figure 9(c)–9(e) demonstrate the wrinkling mode regions corresponding to $h_{VE}/h_{SC} = 2$, $h_{VE}/h_{SC} = 3.5$, and $h_{VE}/h_{SC} = 5$, respectively. As demonstrated in Figs. 9(a)–9(c), when the intermediate layer, VE, is not much thicker than the topmost layer, SC, e.g., $h_{VE}/h_{SC} = 2$, the VE and DE tend to function as a composite substrate and the only active wrinkling mode would be mode II. However, for greater h_{VE}/h_{SC} ratios, e.g., $h_{VE}/h_{SC} = 3.5$ and $h_{VE}/h_{SC} = 5$ as shown in Fig. 9, both modes are possible, depending on the elastic modulus of the layers. Regardless of the wrinkling mode, an increase in the relative thickness of the intermediate layer (h_{VE}/h_{SC}) results in larger critical strains and critical wavelengths, as exhibited in Figs. 9(a) and 9(b). Another parameter affecting the wrinkling mode is the dimensionless elastic modulus of the intermediate layer, E_{VE}/E_{SC}. As

shown in Fig. 9, wrinkling mode transformation occurs when the E_{VE}/E_{SC} reaches a certain value. For example, Fig. 9(e) demonstrates that for $h_{VE}/h_{SC} = 5$, wrinkling mode transformation occurs at approximately $E_{VE}/E_{SC} = 0.11$, which means that for $E_{VE}/E_{SC} < 0.11$ mode II is the active instability mode, while for $E_{VE}/E_{SC} > 0.11$ mode I occurs first. This observation is consistent with Fig. 8, where higher values of E_{VE} increase the possibility of wrinkling mode I. Contrary to the VE layer, the stiffness of the DE layer does not significantly influence the wrinkling mode, as depicted in Figs. 9(c)–9(e). This was also observed in Fig. 8 where the wrinkling mode diagrams were approximately the same for different E_{DE} values. Although the stiffness of the substrate, E_{DE}, does not affect the wrinkling mode, it influences the critical strain and critical wavelength. As shown in Figs. 9(a) and 9(b), an increase in E_{DE} results in a higher critical strain and a lower critical wavelength, which means that keeping all the other parameters (h_{VE}, h_{SC}, E_{VE}, E_{SC}) constant, a stiffer DE layer (corresponding to higher densities of collagen fibers) leads to a greater critical strain and produces a shorter wrinkle wavelength.

C. Effect of collagen degradation on the mechanical behavior of skin

Here finite element modeling is used to establish changes in the critical wrinkling wavelength and strain of a compressively strained three-layer composite skin model whose dermal elastic moduli varies with collagen fiber density and average orientation. Based on the model geometries and material properties presented in the linear buckling section of the Methods section, the wrinkling mode in this model remains consistently mode I, where the SC and VE layers collectively buckle on the dermal layer.

Table S1 in the Supplemental Material [87] compares the critical wavelengths calculated by the finite element method (FEM) and the analytical method (AM) for skin models with varying collagen fiber densities and average collagen fiber orientations. This table also shows the percentage of the discrepancy between the two methods (Δ). The average ($n = 42$) discrepancy is 2.17% with a standard deviation of 0.65%. These data are graphically represented in Fig. 10. For all average collagen fiber bundle orientations, reductions in collagen bundle density lengthen the wrinkling wavelength. This result is consistent with observations that pinching of more aged skin results in the formation of larger wrinkles relative to younger skin [14]. Moreover, the orientation of the bundles has a pronounced effect on the critical wavelength. For fixed collagen fiber densities, the wrinkling wavelength increases as the average fiber orientation increasingly varies from the applied compressive loading direction. This result agrees with the *in vivo* characterization of Kraissl lines, where pinching the skin perpendicular to the local collagen bundle orientation results in larger wavelength and amplitude wrinkles relative to pinching parallel to the orientation [89,90]. The difference between the wavelength for 80% and 50% AOs varies in the range of 10%–16%, depending on the orientation of the collagen bundles. When the orientation varies from 0° to 60°, the analytical and the FEM results show a decline in wavelength increase. The analytical results show that the

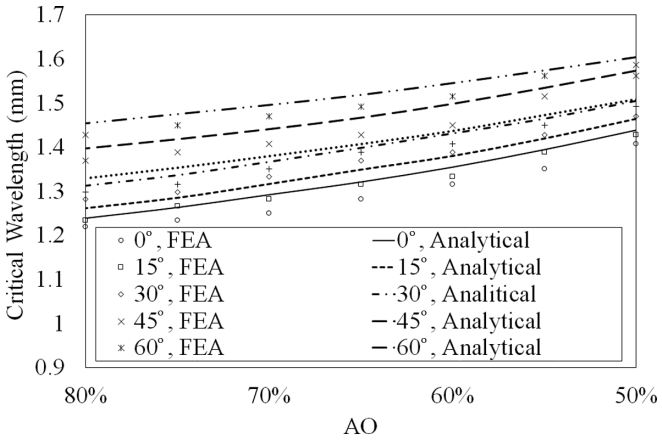

FIG. 10. Critical wavelength vs AO (ratio of the area occupied by bundles to the total area of the matrix) for various orientations of bundles.

lengthening in the wavelength decreases from 16.01% in the case with 0° orientation to 10.28% in the case with 60° orientation. The reduction of collagen fiber density through aging decreases the stiffness of the substrate. This makes the SC layer dominant during bending. Therefore, based on Eq. (9), the wavelength increases. A larger wavelength results in a larger amplitude because the amplitude is proportional to the wavelength. While analytical and finite element results show the same trends, they exhibit small differences. This is most likely attributable to the analytical model employing Euler-Bernoulli beam theory, while no similar assumption is made in the finite element model. Euler-Bernoulli beam theory neglects the shear deformation effect, which results in a systematically higher wavelength compared to the finite element analysis (FEA) results [68]. Considering the change of various other properties of skin such as the thicknesses of its different layers through aging [91], the results of our study cannot be straightforwardly compared with the experimental measurements in the literature. However, despite this limitation, our results can be qualitatively compared with the experimental measurements of wrinkles on human skin. As illustrated in Fig. 10, for a random distribution of collagen fibers, the reduction of collagen fiber density from 80% AO to 50% AO during aging results in a 13.6% increase of critical wavelength. This increase of wavelength with aging is consistent with the study of Kuwazuru *et al.* [92]. They used image processing to measure the wrinkle area of compressed facial skin of female subjects aged 25–56. The parameter "skin wrinkling rate (SWR)" was used to study the difference in skin morphology through aging. They observed a sudden rise in SWR after the age of 30. A larger area of detected wrinkling lines qualitatively corresponds to a larger wrinkle wavelength. Therefore, their measurements show that aged skin experiences longer wavelengths than young skin.

Supplemental Table S2 [87] shows the critical wrinkling strain for varying collagen fiber densities and average fiber orientations away from the compressive loading direction for the FEM and analytical approaches. Critical strain is defined as a strain in which the stress (S11) shows a significant change in the SC layer during the compression process. Similar to Supplemental Table S1 [87], the discrepancy between the

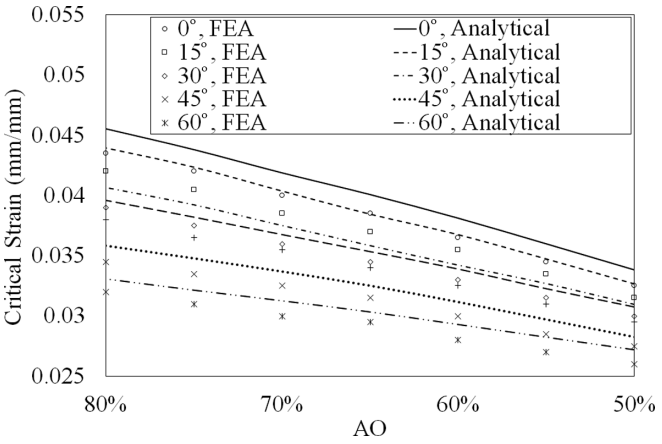

FIG. 11. Critical strain vs AO (ratio of the area occupied by bundles to the total area of the matrix) for various orientations of bundles.

two methods is provided. Figure 11 displays this data graphically. The critical strain for all collagen densities and average fiber orientations falls below strains of $\varepsilon = 0.05$, with the smallest occurring at a strain of $\varepsilon = 0.025$, when fibers are least aligned with the compressive loading axis. This suggests that skin is prone to wrinkling even when subjected to small compressive strains from muscle tension or external stimuli. This is primarily brought about by the discrepancy in elastic modulus between skin layers; a stiff outermost SC adhering to the softer dermal tissue results in wrinkles rather than other surface instabilities [93–95]. Further, for all fiber orientations, the critical strain for wrinkles decreases with age-based degradation of collagen fiber bundle density. An analysis of the critical strain of the cases with 80% AO and 50% AO shows a reduction in the range 17%–26%, depending on the orientation of the collagen bundles. A lower collagen density reduces the stiffness of the substrate and makes the SC the dominant layer during buckling. Therefore, based on Eq. (10), the critical strain has a lower value compared with the 80% AO model. The analytical and FEM results show that the sensitivity of the critical strain decreases while the orientation varies from 0° to 60°. For instance, the analytical results show that the difference between critical strain for 80% AO and 50% AO decreases from 25.70% to 17.78% in the cases with 0° and 60° orientation, respectively. Both the wavelength and critical strain results indicate that the skin with aligned collagen fibers in the tension-compression direction is more sensitive to collagen degradation. We anticipate, therefore, that age-based dermal softening will likely result in skin undergoing larger *in vivo* strains parallel with Langer's lines because of the *in vivo* skin tension. In turn, the Poisson-based lateral contraction orthogonal to the average collagen alignment will readily surpass the critical wrinkling strain, resulting in wrinkling. Certainly, this would explain the alignment of wrinkles with Langer's lines [96]. It is worth noting, however, that critical wrinkling strain is not only dependent on the collagen density. Other parameters such as thickness and individual layer material properties will be influential [11,16]. However, these parameters are not examined in this study. Moreover, pretension or residual stresses have been ignored here because the dependency of residual stress on collagen fiber orientation remains unclear. Experimental studies exploring this relationship exhibit contradictory results regarding the expansion or shrinkage of excised specimens [59,97–99], signs of the inherent tensile or compressive stresses. Nonetheless, while these inherent stresses may act to cause wrinkling, they do not affect the critical strains detailed here.

The results detailed in Figs. 10 and 11 are valid for small compressive strains that result in sinusoidal wrinkles. For larger compressive strains, however, Eqs. (9) and (10) are no longer valid, and only the nonlinear finite element model can capture the postbuckling topographies.

D. Effect of collagen degradation on the postbuckling behavior of skin

The results detailed in Figs. 10 and 11 are valid only for small compressive strains resulting in symmetrical sinusoidal wrinkles. For larger compressive strains, Eqs. (9) and (10) are no longer valid, and only a nonlinear model can capture the postbuckling topographies. Figures 12(a) and 12(b) show how a three-layer skin model with two different densities of collagen bundles responds to a large compressive strain. The color bar depicts the deformation along the Y axis. Zoomed images show that collagen bundles buckle inside the ground substance. An individual fiber is created using multiple truss elements inside the matrix. In the absence of the matrix, a single fiber, meshed with multiple truss elements, cannot resist the compression load. However, in the presence of the matrix, because fibers are embedded in the matrix they can resist compression. Collagen bundles in the model can buckle because an individual collagen bundle is meshed with multiple truss elements. The truss elements embedded in the matrix can rotate around their shared nodes to model the buckling. Figure 12(c) shows the profile of the outer layer of the deformed skin with 0° orientation and 80% and 50% AOs. Figure 12 indicates that a reduction in collagen fiber density results in larger wavelength and amplitude folding patterns, consistent with the larger and deeper wrinkles that form in aged skin [92]. Big wrinkles can penetrate to the dermal layer and induce large bending stresses and possibly damage the dermis.

Figure 13 shows the calculated roughness parameters after 30% compressive strain for the cases with different orientations with 80% and 50% AOs of collagen bundles in the dermal layer. Here, the roughness is a representation of the wrinkles' amplitudes. As depicted in Figs. 13(a) and 13(b), both average roughness (R_a) and root mean square roughness (R_q) are smaller for younger skins (80% AO) compared to older ones (50% AO). The roughness increases between cases with 80% and 50% AOs by 13.5% and 18.9% according to R_a and R_q parameters, respectively. For a random distribution of collagen fibers, R_a and R_q of the old skin are 18% and 25% higher than the young one. This result is consistent with the observation of Trojahn *et al.* [100]. They measured the roughness parameters of 38 male and female volunteers of three age groups (14 children, 12 younger adults, and 12 older adults). For most of the roughness parameters measured in their study, differences between age groups were statistically significant. Average roughness was about 10% higher in younger adults compared to children, and about 50% higher in older adults compared to younger adults.

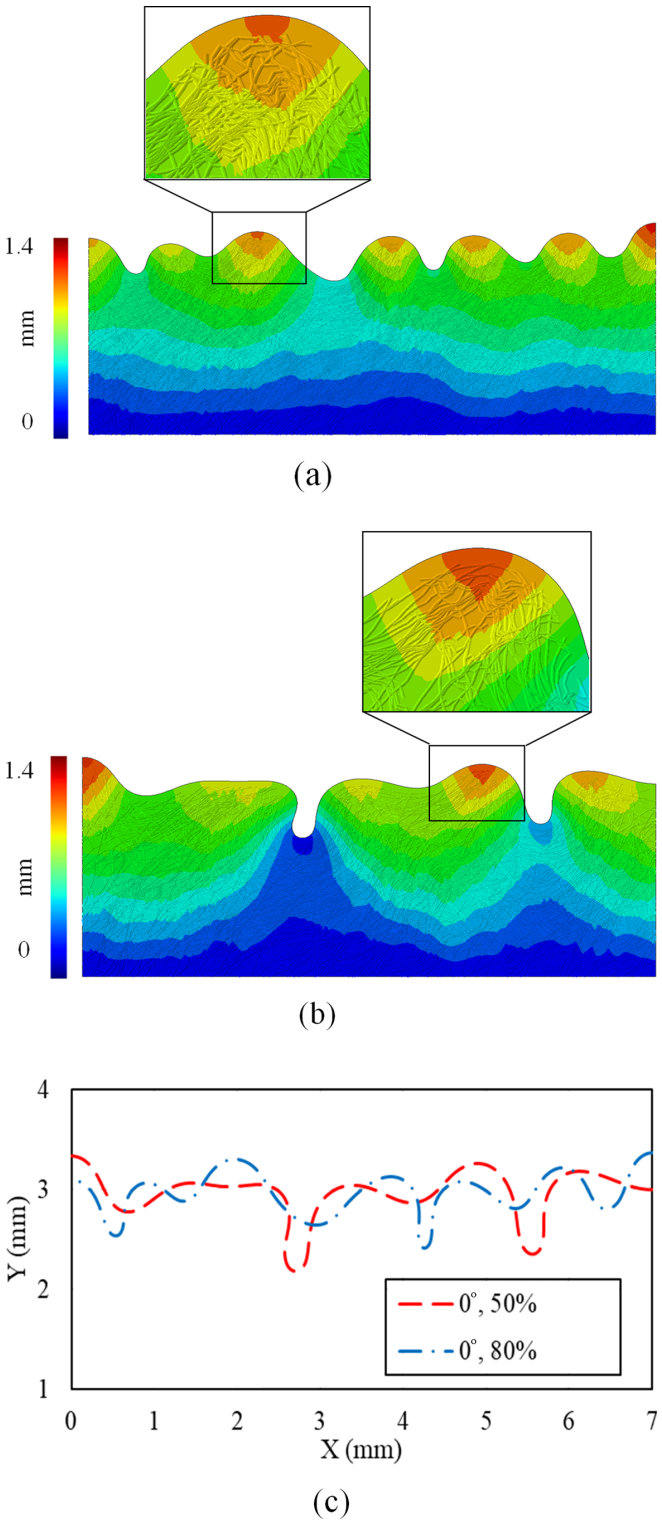

FIG. 12. Wrinkled skin under 30% compressive strain with 0° orientation and with (a) 80% AO and (b) 50% AO inside the dermal layer. (c) Comparison between the profiles of the wrinkles after deformation.

E. Limitations of the study

The models we employ in this work incorporate simplifications and limitations that prevent them from accurately capturing the complex nonlinearity, anisotropy, heterogeneity,

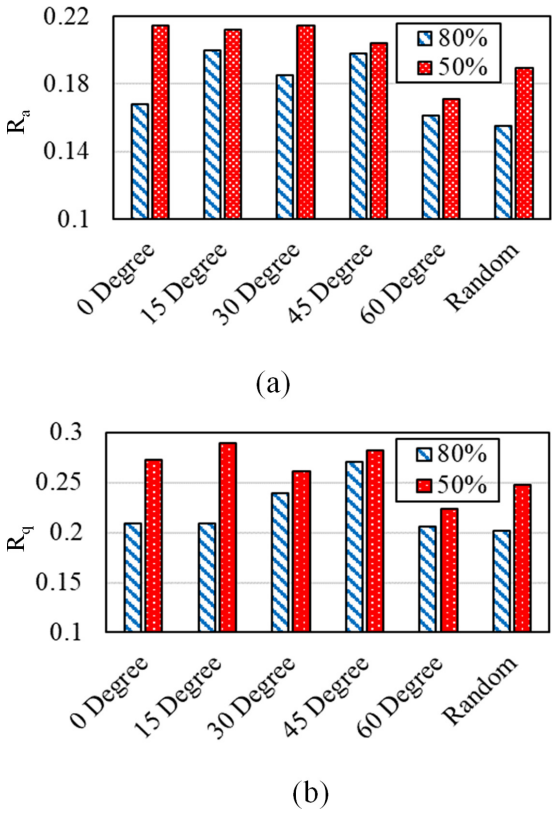

FIG. 13. Variation of (a) R_a (average roughness) and (b) R_q (root mean square roughness) in cases with different orientations and with 80% and 50% AOs in the dermal layer. The unit of R_a and R_q is mm.

and viscoelasticity of human skin. In the analytical method, the Euler-Bernoulli beam theory that has been assumed does not account for shear strain and unrealistically considers the dermal layer to be infinite in size. In the computational models, collagen bundles were modeled with straight truss elements without any interaction between crossing bundles, unlike actual dermal tissue that contains tortuous and intertwined collagen fibers. Moreover, except for the equivalent elastic modulus of the dermis, all other age-dependent geometrical and material properties of the skin model are fixed. In reality, the thickness of the stratum corneum, viable epidermis, and the diameter of the collagen bundles and their mechanical properties also alter with age [4,5,7]. The effect of the residual stress of natural skin was not considered in the models [101–103]. In a part of this study, linear elasticity was assumed for all tissue layers to enable comparisons of analytical and computational results. We recognize that hyperelastic and hyperviscoelastic material models provide more accurate predictions of the mechanical behavior of the skin [12,16,58,60,104–106]. In our two-dimensional study, it was only possible to consider the in-plane orientation of collagen bundles. However, apparently there is a three-dimensional distribution of collagen bundles inside the dermal layer [107].

Despite all these simplifications, the developed models provide a clear indication of age-induced mechanical degradation of dermal tissue, and how this leads to the development of wrinkles. Nonetheless, more extensive experimental and computational studies employing more accurate skin parameters should be completed to build upon the results presented here.

IV. CONCLUSION

The dermal layer of skin is largely composed of collagen fiber bundles, which provide structural strength and elasticity. Extensive collagen fragmentation and degradation have been observed in aged or photodamaged skin. In this paper, analytical and computational methods are used to examine how age-induced degradation of collagen fiber bundles in dermal tissue affects the mechanical behavior of skin, resulting in the promotion of wrinkles. The results of the study show that despite the orientation of bundles, the elastic modulus of the dermal layer decreases with age, with the effect of collagen fiber bundle degradation occurring more strongly when aligned with the loading axis. Results further show that age-based dermal softening results in an increase in wrinkling critical wavelength. This critical wavelength varies notably with fiber bundle orientation. Moreover, the critical wrinkling strain decreases both with age and misalignment of the collagen bundle orientation to the loading axis, making aged skin more susceptible to wrinkling from smaller compressive stimuli. Finally, finite element postbuckling analyses show that the elastic modulus of the dermis, which is dependent on the density of collagen bundles, regulates the wrinkle patterns of the compressed skin in high strains. These results provide insight into the mechanistic process of softening SC or stiffening dermis to reduce signs of aging. It also reveals mechanistic insight useful for advancing cosmetic antiaging formulations, where stiffening of the dermis, or softening of SC is needed to alleviate wrinkles and reduce signs of aging.

The complete data supporting the results discussed in this study are available from the corresponding author upon reasonable request.

ACKNOWLEDGMENTS

M.R., P.C., and A.H.F acknowledge the support from the Binghamton University start-up research funding. This material is based upon work supported by the National Science Foundation, USA under Grant No. 1653071. We also thank the anonymous reviewers for their constructive comments and suggestions. This work, for a part of the computational simulations, used the Extreme Science and Engineering Discovery Environment (XSEDE), which is supported by National Science Foundation.

M.J.R. designed the study. P.C., N.D. and A.H.F performed histology, developed models, and analyzed results. M.J.R., P.C., G.K.G., and A.H.F wrote the manuscript and discussed the results.

The authors declare no competing interests.

APPENDIX

To calculate the critical strain and critical wavelength of mode II, the governing equation for deflection of a single layer beam (the SC) resting on a composite two-layer foundation (composed of the VE and DE) is

$$E^*_{\mathrm{SC}} I_{\mathrm{SC}} \frac{d^4 w}{dx^4} + F \frac{d^2 w}{dx^2} + K_e w = 0, \tag{A1}$$

where $I_{\mathrm{SC}} = h^3_{\mathrm{SC}}/12$ and K_e is the effective stiffness of the composite foundation. To find the effective stiffness of the composite substrate, K_e, the substrate is considered to have a distributed pressure $p(x)$, induced in the interface of the substrate with the top layer. There is an analytical solution for the displacement of the surface of the foundation under this normal stress $p = p_0 \cos(\omega_{\mathrm{II}} x)$, where p_0 and ω_{II} are the amplitude and the angular frequency of the distributed pressure, respectively. Then, the effective stiffness for the composite foundation is obtained as

$$K_e = \frac{p}{u_y}. \tag{A2}$$

According to Porter *et al.* [108] the deflection of the upper surface of the substrate is obtained as

$$u_y = -\frac{1}{\pi \mu_2} \int_0^\infty \{[0.5(\kappa_2 - 1)B - C - D\omega h_{\mathrm{VE}}]\cosh\omega h_2 + [-A - B\omega h_{\mathrm{VE}} + 0.5(\kappa_2 - 1)D]\sinh\omega h_2\} \times \tilde{p}_c(\omega) \frac{\cos(\omega x)}{\omega} d\omega, \tag{A3}$$

where

$$\tilde{p}_c(\omega) = \int_0^\infty p(x)\cos(\omega x) dx, \tag{A4}$$

$$A = P(QB + RD), \tag{A5}$$

$$B = \frac{(PR+1)\sinh(\omega h_{\mathrm{VE}}) - (PQ - \omega h_{\mathrm{VE}})\cosh(\omega h_{\mathrm{VE}})}{(\omega h_{\mathrm{VE}})^2 - PS(PR+1) + P(S-R)\cosh^2(\omega h_{\mathrm{VE}}) + PQ[\sinh(2\omega h_{\mathrm{VE}}) - PQ]}, \tag{A6}$$

$$C = P(SB - QD), \tag{A7}$$

$$D = \frac{-(Ps+1)\cosh(\omega h_{\mathrm{VE}}) - (PQ + \omega h_{\mathrm{VE}})\sinh(\omega h_{\mathrm{VE}})}{(\omega h_{\mathrm{VE}})^2 - PS(PR+1) + P(S-R)\cosh^2(\omega h_{\mathrm{VE}}) + PQ[\sinh(2\omega h_{\mathrm{VE}}) - PQ]}, \tag{A8}$$

$$\kappa_2 = 3 - 4\nu_{\mathrm{VE}}, \tag{A9}$$

$$\mu_2 = \frac{E_{\mathrm{VE}}}{2(1+\upsilon_{\mathrm{VE}})}, \tag{A10}$$

$$P = \frac{1}{4(\beta - \alpha)(1+\beta)}, \tag{A11}$$

$$R = (1-\alpha)(\alpha - 1 - 2\beta), \tag{A12}$$

$$S = (1+\alpha)^2 + 2\beta(\alpha - 1 - 2\beta), \tag{A13}$$

where α and β, the Dundurs constants, are

$$\alpha = \frac{\zeta(\kappa_s + 1) - (\kappa_2 + 1)}{\zeta(\kappa_s + 1) + (\kappa_2 + 1)}, \tag{A14}$$

$$\beta = \frac{\zeta(\kappa_s - 1) - (\kappa_2 - 1)}{\zeta(\kappa_s + 1) + (\kappa_2 + 1)}, \tag{A15}$$

$$\kappa_s = 3 - 4\upsilon_{\mathrm{DE}}, \tag{A16}$$

$$\zeta = \frac{\mu_2}{\mu_s}, \tag{A17}$$

$$\mu_s = \frac{E_{\mathrm{DE}}}{2(1 + \upsilon_{\mathrm{DE}})}. \tag{A18}$$

Assuming the beam deflection to be $w = W_0 \cos(2\pi x/\lambda_1)$, the force can be derived from the governing equation as

$$F = E^*_{\mathrm{SC}} I_{\mathrm{SC}} \omega_{\mathrm{II}}^2 - \frac{2\mu_2}{\vartheta\, \omega_{\mathrm{II}}}. \tag{A19}$$

Similar to the first wrinkling mode, the critical wrinkling wavelength of the second mode of wrinkling should satisfy this condition:

$$\frac{\partial F}{\partial \omega_{\mathrm{II}}} = 0. \tag{A20}$$

Hence, the critical compressive strain for wrinkling mode II becomes

$$\varepsilon_c^{\mathrm{II}} = \frac{F_c^{\mathrm{II}}}{E^*_{\mathrm{SC}} h_{\mathrm{SC}}}. \tag{A21}$$

[1] Z. W. Lipsky, C. N. H. Marques, and G. K. German, Lipid depletion enables permeation of *Staphylococcus aureus* bacteria through human stratum corneum, Tissue Barriers **8**, 1754706 (2020).

[2] A. V. Rawlings and C. R. Harding, Moisturization and skin barrier function, Dermatol. Ther. **17 Suppl 1**, 43 (2004).

[3] W. Montagna, *The Structure and Function of Skin*, 3rd ed. (Academic, New York, 1974).

[4] D. J. Tobin, Introduction to skin aging, J. Tissue Viability **26**, 37 (2017).

[5] V. Marcos-Garcés, P. Molina Aguilar, C. Bea Serrano, V. García Bustos, J. Benavent Seguí, A. Ferrández Izquierdo, and A. Ruiz-Saurí, Age-related dermal collagen changes during development, maturation and ageing—a morphometric and comparative study, J. Anat. **225**, 98 (2014).

[6] J. Sandby-Møller, T. Poulsen, and H. C. Wulf, Epidermal thickness at different body sites: Relationship to age, gender, pigmentation, blood content, skin type and smoking habits, Acta Derm. Venereol. **83**, 410 (2003).

[7] M. A. Farage, K. W. Miller, P. Elsner, and H. I. Maibach, Structural characteristics of the aging skin: A review, Cutaneous Ocul. Toxicol. **26**, 343 (2007).

[8] C. Edwards and R. Marks, Evaluation of biomechanical properties of human skin, Clin. Dermatol. **13**, 375 (1995).

[9] H. Joodaki and M. B. Panzer, Skin mechanical properties and modeling: A review, Proc. Inst. Mech. Eng., Part H **232**, 323 (2018).

[10] A. Kalra, A. Lowe, and A. M. Al-Jumally, Mechanical behaviour of skin: A review, J. Mater. Sci. Eng. **5**, (2016).

[11] P. Chavoshnejad, S. More, and M. J. Razavi, From surface microrelief to big wrinkles in skin: A mechanical *in-silico* model, (2020).

[12] G. Limbert, Mathematical and computational modelling of skin biophysics: A review, Proc. R. Soc. London, Ser. A **473**, 20170257 (2017).

[13] Y. Shiihara, M. Sato, Y. Hara, I. Iwai, and N. Yoshikawa, Microrelief suppresses large wrinkling appearance: An *in silico* study, Skin Res. Technol. **21**, 184 (2015).

[14] N. Magnenat-Thalmann, P. Kalra, J. L. Lévêque, R. Bazin, D. Batisse, and B. Querleux, A computational skin model: Fold and wrinkle formation, IEEE Trans. Inf. Technol. Biomed. **6**, 317 (2002).

[15] C. Flynn and B. A. O. McCormack, Finite element modelling of forearm skin wrinkling, Skin Res. Technol. **14**, 261 (2008).

[16] G. Limbert and E. Kuhl, On skin microrelief and the emergence of expression micro-wrinkles, Soft Matter **14**, 1292 (2018).

[17] M. F. Leyva-Mendivil, A. Page, N. W. Bressloff, and G. Limbert, A mechanistic insight into the mechanical role of the stratum corneum during stretching and compression of the skin, J. Mech. Behav. Biomed. Mater. **49**, 197 (2015).

[18] I. L. Kruglikov and P. E. Scherer, Skin aging as a mechanical phenomenon: The main weak links, Nutr. Healthy Aging **4**, 291 (2018).

[19] J. W. Y. Jor, M. D. Parker, A. J. Taberner, M. P. Nash, and P. M. F. Nielsen, Computational and experimental characterization of skin mechanics: Identifying current challenges and future directions, Wiley Interdiscip. Rev.: Syst. Biol. Med. **5**, 539 (2013).

[20] K. Robertson and J. L. Rees, Variation in epidermal morphology in human skin at different body sites as measured by reflectance confocal microscopy, Acta Derm. Venereol. **90**, 368 (2010).

[21] D. Batisse, R. Bazin, and T. Baldeweck, Influence of age on the wrinkling capacities of skin, Skin Res. Technol. **8**, 148 (2002).

[22] Y. Takema, Y. Yorimoto, M. Kawai, and G. Imokawa, Age-related changes in the elastic properties and thickness of human facial skin, Br. J. Dermatol. **131**, 641 (1994).

[23] A. Kalra, A. Lowe, and A. A. Jumaily, An overview of factors affecting the skin's Young's modulus, J. Ageing Sci. **4**, 1000156 (2016).

[24] C. Li, G. Guan, R. Reif, Z. Huang, and R. K. Wang, Determining elastic properties of skin by measuring surface waves from an impulse mechanical stimulus using phase-sensitive optical coherence tomography, J. R. Soc. Interface **9**, 831 (2012).

[25] Y. Hara, Y. Masuda, T. Hirao, and N. Yoshikawa, The relationship between the Young's modulus of the stratum corneum and age: A pilot study, Skin Res. Technol. **19**, 339 (2013).

[26] Y. S. Papir, K. H. Hsu, and R. H. Wildnauer, The mechanical properties of stratum corneum. I. The effect of water and ambient temperature on the tensile properties of newborn rat stratum corneum, Biochim. Biophys. Acta **399**, 170 (1975).

[27] F. H. Silver, J. W. Freeman, and D. DeVore, Viscoelastic prop-

erties of human skin and processed dermis, Skin Res. Technol. **7**, 18 (2001).

[28] H. Zahouani, C. Pailler-Mattei, B. Sohm, R. Vargiolu, V. Cenizo, and R. Debret, Characterization of the mechanical properties of a dermal equivalent compared with human skin *in vivo* by indentation and static friction tests, Skin Res. Technol. **15**, 68 (2009).

[29] X. Liu, J. Cleary, and G. K. German, The global mechanical properties and multi-scale failure mechanics of heterogeneous human stratum corneum, Acta Biomater. **43**, 78 (2016).

[30] N. Dhandapani, K. Samuelsson, M. Sköld, K. Zohrevand, and G. K. German, Mechanical, compositional, and microstructural changes caused by human skin maceration, Extreme Mech. Lett. **41**, 101017 (2020).

[31] C. Flynn and B. A. O. McCormack, Simulating the wrinkling and aging of skin with a multi-layer finite element model, J. Biomech. **43**, 442 (2010).

[32] N. A. Fenske and C. W. Lober, Structural and functional changes of normal aging skin, J. Am. Acad. Dermatol. **15**, 571 (1986).

[33] H. S. Ryu, Y. H. Joo, S. O. Kim, K. C. Park, and S. W. Youn, Influence of age and regional differences on skin elasticity as measured by the cutometer, Skin Res. Technol. **14**, 354 (2008).

[34] L. Rittié and G. J. Fisher, Natural and sun-induced aging of human skin, Cold Spring Harbor Perspect. Med. **5**, a015370 (2015).

[35] N. M. Craven, R. E. Watson, C. J. Jones, C. A. Shuttleworth, C. M. Kielty, and C. E. Griffiths, Clinical features of photodamaged human skin are associated with a reduction in collagen VII, Br. J. Dermatol. **137**, 344 (1997).

[36] T. T. Nguyen, C. Eklouh-Molinier, D. Sebiskveradze, J. Feru, C. Terryn, M. Manfait, S. Brassart-Pasco, and O. Piot, Changes of skin collagen orientation associated with chronological aging as probed by polarized-FTIR micro-imaging, Analyst **139**, 2482 (2014).

[37] R. Maidhof, E. Knapp, F. Liebel, M. Fair, and E. H. Rubinson, Technical approaches to select high-performance instant skin smoothing formulations: Correlation of *in vitro* and *in vivo* assessment methods, Skin Res. Technol. **25**, 606 (2019).

[38] M. Pensalfini, M. Rotach, R. Hopf, A. Bielicki, R. Santoprete, and E. Mazza, How cosmetic tightening products modulate the biomechanics and morphology of human skin, Acta Biomater. **115**, 299 (2020).

[39] G. Limbert, Investigating the influence of relative humidity on expression microwrinkles, J. Aesthetic Nurs. **7**, 204 (2018).

[40] Z. W. Lipsky and G. K. German, Ultraviolet light degrades the mechanical and structural properties of human stratum corneum, J. Mech. Behav. Biomed. Mater. **100**, 103391 (2019).

[41] M. Yaar and B. A. Gilchrest, Photoageing: Mechanism, prevention and therapy, Br. J. Dermatol. **157**, 874 (2007).

[42] O. S. Kwon, H. G. Yoo, J. H. Han, S. R. Lee, J. H. Chung, and H. C. Eun, Photoaging-associated changes in epidermal proliferative cell fractions in vivo, Arch. Dermatol. Res. **300**, 47 (2008).

[43] I. Hadshiew, Skin aging and photoaging: The role of DNA damage and repair, Am. J. Contact Dermat. **11**, 19 (2000).

[44] A. P. Schuch, N. C. Moreno, N. J. Schuch, C. F. M. Menck, and C. C. M. Garcia, Sunlight damage to cellular DNA: Focus on oxidatively generated lesions, Free Radic. Biol. Med. **107**, 110 (2017).

[45] U. Panich, G. Sittithumcharee, N. Rathviboon, and S. Jirawatnotai, Ultraviolet radiation-induced skin aging: The role of DNA damage and oxidative stress in epidermal stem cell damage mediated skin aging, Stem Cells Int. **2016**, 7370642 (2016).

[46] A. Villaret, C. Ipinazar, T. Satar, E. Gravier, C. Mias, E. Questel, A.-M. Schmitt, V. Samouillan, F. Nadal, and G. Josse, Raman characterization of human skin aging, Skin Res. Technol. **25**, 270 (2019).

[47] L. Baumann, Skin ageing and its treatment, J. Pathol. **211**, 241 (2007).

[48] R. Tang, V. Samouillan, J. Dandurand, C. Lacabanne, M.-H. Lacoste-Ferre, P. Bogdanowicz, P. Bianchi, A. Villaret, and F. Nadal-Wollbold, Identification of ageing biomarkers in human dermis biopsies by thermal analysis (DSC) combined with Fourier transform infrared spectroscopy (FTIR/ATR), Skin Res. Technol. **23**, 573 (2017).

[49] S. Shuster, M. M. Black, and E. McVitie, The influence of age and sex on skin thickness, skin collagen and density, Br. J. Dermatol. **93**, 639 (1975).

[50] T. Quan and G. J. Fisher, Role of age-associated alterations of the dermal extracellular matrix microenvironment in human skin aging: A mini-review, Gerontology **61**, 427 (2015).

[51] M. Gniadecka, O. F. Nielsen, S. Wessel, M. Heidenheim, D. H. Christensen, and H. C. Wulf, Water and protein structure in photoaged and chronically aged skin, J. Invest. Dermatol. **111**, 1129 (1998).

[52] G. J. Fisher, Z. Q. Wang, S. C. Datta, J. Varani, S. Kang, and J. J. Voorhees, Pathophysiology of premature skin aging induced by ultraviolet light, N. Engl. J. Med. **337**, 1419 (1997).

[53] J. Varani, M. K. Dame, L. Rittie, S. E. G. Fligiel, S. Kang, G. J. Fisher, and J. J. Voorhees, Decreased collagen production in chronologically aged skin: Roles of age-dependent alteration in fibroblast function and defective mechanical stimulation, Am. J. Pathol. **168**, 1861 (2006).

[54] C. O. Flynn and B. A. O. McCormack, A three-layer model of skin and its application in simulating wrinkling, Comput. Methods Biomech. Biomed. Eng. **12**, 125 (2009).

[55] Y. Zhao, B. Feng, J. Lee, N. Lu, and D. M. Pierce, A multi-layered computational model for wrinkling of human skin predicts aging effects, J. Mech. Behav. Biomed. Mater. **103**, 103552 (2020).

[56] Y. Zhao, B. Feng, J. Lee, N. Lu, and D. M. Pierce, A multi-layered model of human skin elucidates mechanisms of wrinkling in the forehead, J. Mech. Behav. Biomed. Mater. **105**, 103694 (2020).

[57] D. Pond, A. T. McBride, L. M. Davids, B. D. Reddy, and G. Limbert, Microstructurally-based constitutive modelling of the skin—Linking intrinsic ageing to microstructural parameters, J. Theor. Biol. **444**, 108 (2018).

[58] A. Ní Annaidh, K. Bruyère, M. Destrade, M. D. Gilchrist, C. Maurini, M. Otténio, and G. Saccomandi, Automated estimation of collagen fibre dispersion in the dermis and its contribution to the anisotropic behaviour of skin, Ann. Biomed. Eng. **40**, 1666 (2012).

[59] A. Ní Annaidh, K. Bruyère, M. Destrade, M. D. Gilchrist, and M. Otténio, Characterization of the anisotropic mechanical

properties of excised human skin, J. Mech. Behav. Biomed. Mater. **5**, 139 (2012).

[60] D. Garcia-Gonzalez, A. Jérusalem, S. Garzon-Hernandez, R. Zaera, and A. Arias, A continuum mechanics constitutive framework for transverse isotropic soft tissues, J. Mech. Phys. Solids **112**, 209 (2018).

[61] D. Laiacona, J. M. Cohen, K. Coulon, Z. W. Lipsky, C. Maiorana, R. Boltyanskiy, E. R. Dufresne, and G. K. German, Non-invasive *in vivo* quantification of human skin tension lines, Acta Biomater. **88**, 141 (2019).

[62] E. Dupont, J. Gomez, and D. Bilodeau, Beyond UV radiation: A skin under challenge, Int. J. Cosmet. Sci. **35**, 224 (2013).

[63] K. Jariashvili, B. Madhan, B. Brodsky, A. Kuchava, L. Namicheishvili, and N. Metreveli, UV damage of collagen: Insights from model collagen peptides, Biopolymers **97**, 189 (2012).

[64] P. P. van Zuijlen, H. J. de Vries, E. N. Lamme, J. E. Coppens, J. van Marle, R. W. Kreis, and E. Middelkoop, Morphometry of dermal collagen orientation by Fourier analysis is superior to multi-observer assessment, J. Pathol. **198**, 284 (2002).

[65] O. S. Osman, J. L. Selway, P. E. Harikumar, C. J. Stocker, E. T. Wargent, M. A. Cawthorne, S. Jassim, and K. Langlands, A novel method to assess collagen architecture in skin, BMC Bioinf. **14**, 260 (2013).

[66] H. G. Allen, *Analysis and Design of Structural Sandwich Panels* (Elsevier, Amsterdam, 1969).

[67] R. Vescovini, M. D'Ottavio, L. Dozio, and O. Polit, Buckling and wrinkling of anisotropic sandwich plates, Int. J. Eng. Sci. **130**, 136 (2018).

[68] F. Jia, Y.-P. Cao, T.-S. Liu, Y. Jiang, X.-Q. Feng, and S.-W. Yu, Wrinkling of a bilayer resting on a soft substrate under in-plane compression, Philos. Mag. **92**, 1554 (2012).

[69] E. Lejeune, A. Javili, and C. Linder, An algorithmic approach to multi-layer wrinkling, Extreme Mech. Lett. **7**, 10 (2016).

[70] F. Brau, H. Vandeparre, A. Sabbah, C. Poulard, A. Boudaoud, and P. Damman, Multiple-length-scale elastic instability mimics parametric resonance of nonlinear oscillators, Nat. Phys. **7**, 56 (2011).

[71] A. J. Nolte, N. Takane, E. Hindman, W. Gaynor, M. F. Rubner, and R. E. Cohen, Thin film thickness gradients and spatial patterning via salt etching of polyelectrolyte multilayers, Macromolecules **40**, 5479 (2007).

[72] R. Huang, C. M. Stafford, and B. D. Vogt, Effect of surface properties on wrinkling of ultrathin films, J. Aerosp. Eng. **20**, 38 (2007).

[73] A. L. Volynskii, S. Bazhenov, O. V. Lebedeva, and N. F. Bakeev, Mechanical buckling instability of thin coatings deposited on soft polymer substrates, J. Mater. Sci. **35**, 547 (2000).

[74] S. Cai, D. Breid, A. J. Crosby, Z. Suo, and J. W. Hutchinson, Periodic patterns and energy states of buckled films on compliant substrates, J. Mech. Phys. Solids **59**, 1094 (2011).

[75] ABAQUS Analysis User's Manual, Version 6.13 (Dassault System Simula Corp, Johnston, RI, 2013).

[76] T. Belytschko, J. Fish, and B. E. Engelmann, A finite element with embedded localization zones, Comput. Methods Appl. Mech. Eng. **70**, 59 (1988).

[77] J. Fish and T. Belytschko, Elements with embedded localization zones for large deformation problems, Comput. Struct. **30**, 247 (1988).

[78] S. A. Tabatabaei, S. V. Lomov, and I. Verpoest, Assessment of embedded element technique in meso-FE modelling of fibre reinforced composites, Compos. Struct. **107**, 436 (2014).

[79] S. Lin, L. Hapach, C. Reinhart-King, and L. Gu, Towards tuning the mechanical properties of three-dimensional collagen scaffolds using a coupled fiber-matrix model, Materials **8**, 5376 (2015).

[80] S. A. Yousefsani, F. Farahmand, and A. Shamloo, A three-dimensional micromechanical model of brain white matter with histology-informed probabilistic distribution of axonal fibers, J. Mech. Behav. Biomed. Mater. **88**, 288 (2018).

[81] P. Chavoshnejad and M. J. Razavi, Effect of the interfiber bonding on the mechanical behavior of electrospun fibrous mats, Sci. Rep. **10**, 7709 (2020).

[82] P. Chavoshnejad, O. Alsmairat, and C. Ke, Effect of interfiber bonding on the rupture of electrospun fibrous mats, J. Phys. Appl. Phys. **54**, 025302 (2021).

[83] C. Berkey, K. Biniek, and R. H. Dauskardt, Predicting hydration and moisturizer ingredient effects on mechanical behavior of human stratum corneum, Extreme Mech. Lett. **46**, 101327 (2021).

[84] X. Liu and G. K. German, Measuring and modeling contractile drying in human stratum corneum, J. Vis. Exp. (2017), doi: 10.3791/55336.

[85] K. Langer, On the anatomy and physiology of the skin. I. The cleavability of the cutis. (Translated from Langer, K. (1861). Zur Anatomie und Physiologie der Haut. I. Uber die Spaltbarkeit der Cutis. Sitzungsbericht der Mathematisch-naturwissenschaftlichen Classe der Kaiserlichen Academie der Wissenschaften, **44**, 19.), Br. J. Plast. Surg. **31**, 3 (1978).

[86] S. Aarabi, K. A. Bhatt, Y. Shi, J. Paterno, E. I. Chang, S. A. Loh, J. W. Holmes, M. T. Longaker, H. Yee, and G. C. Gurtner, Mechanical load initiates hypertrophic scar formation through decreased cellular apoptosis, FASEB J. **21**, 3250 (2007).

[87] See Supplemental Material at http://link.aps.org/supplemental/10.1103/PhysRevE.104.034406 for details of the elastic modulus, critical wavelength, and critical stain of the model.

[88] O. Kuwazuru, J. Saothong, and N. Yoshikawa, Mechanical approach to aging and wrinkling of human facial skin based on the multistage buckling theory, Med. Eng. Phys. **30**, 516 (2008).

[89] B. J. Wilhelmi, S. J. Blackwell, and L. G. Phillips, Langer's lines: To use or not to use, Plast. Reconstr. Surg. **104**, 208 (1999).

[90] A. F. Borges, Relaxed skin tension lines (RSTL) versus other skin lines, Plast. Reconstr. Surg. **73**, 144 (1984).

[91] M. C. Branchet, S. Boisnic, C. Frances, and A. M. Robert, Skin thickness changes in normal aging skin, Gerontology **36**, 28 (1990).

[92] O. Kuwazuru, K. Miyamoto, N. Yoshikawa, and S. Imayama, Skin wrinkling morphology changes suddenly in the early 30s, Skin Res. Technol. **18**, 495 (2012).

[93] S. Budday, S. Andres, B. Walter, P. Steinmann, and E. Kuhl, Wrinkling instabilities in soft bilayered systems, Philos. Trans. R. Soc., A **375**, 20160163 (2017).

[94] Q. Wang and X. Zhao, Beyond wrinkles: Multimodal surface instabilities for multifunctional patterning, MRS Bull. **41**, 115 (2016).

[95] P. S. Stewart, S. L. Waters, T. El Sayed, D. Vella, and A.

Goriely, Wrinkling, creasing, and folding in fiber-reinforced soft tissues, Extreme Mech. Lett. **8**, 22 (2016).

[96] T. Yasui, Y. Takahashi, S. Fukushima, Y. Ogura, T. Yamashita, T. Kuwahara, T. Hirao, and T. Araki, Observation of dermal collagen fiber in wrinkled skin using polarization-resolved second-harmonic-generation microscopy, Opt. Express **17**, 912 (2009).

[97] M. D. Ridge and V. Wright, The directional effects of skin. A bio-engineering study of skin with particular reference to Langer's lines, J. Invest. Dermatol. **46**, 341 (1966).

[98] L. H. Jansen and P. B. Rottier, Comparison of the mechanical properties of strips of human abdominal skin excised from below and from above the umbilic, Dermatology **117**, 252 (1958).

[99] J. W. Y. Jor, P. M. F. Nielsen, M. P. Nash, and P. J. Hunter, Modelling collagen fibre orientation in porcine skin based upon confocal laser scanning microscopy: Modelling collagen fibre orientation, Skin Res. Technol. **17**, 149 (2011).

[100] C. Trojahn, G. Dobos, M. Schario, L. Ludriksone, U. Blume-Peytavi, and J. Kottner, Relation between skin microtopography, roughness, and skin age, Skin Res. Technol. **21**, 69 (2015).

[101] H. Alexander and T. H. Cook, Accounting for natural tension in the mechanical testing of human skin, J. Invest. Dermatol. **69**, 310 (1977).

[102] C. Flynn, A. Taberner, and P. Nielsen, Mechanical characterisation of *in vivo* human skin using a 3D force-sensitive micro-robot and finite element analysis, Biomech. Model. Mechanobiol. **10**, 27 (2011).

[103] D. R. Veronda and R. A. Westmann, Mechanical characterization of skin—finite deformations, J. Biomech. **3**, 111 (1970).

[104] R. B. Groves, S. A. Coulman, J. C. Birchall, and S. L. Evans, An anisotroic hyperelastic model for skin: Experimental measurements, finite element modelling and identification of parameters for human and murine skin, J. Mech. Behav. Biomed. Mater. **18**, 167 (2013).

[105] H. Jayabal, N. N. Dingari, and B. Rai, A linear viscoelastic model to understand skin mechanical behaviour and for cosmetic formulation design, Int. J. Cosmet. Sci. **41**, 292 (2019).

[106] F. Khatyr, C. Imberdis, P. Vescovo, D. Varchon, and J.-M. Lagarde, Model of the viscoelastic behaviour of skin *in vivo* and study of anisotropy, Skin Res. Technol. **10**, 96 (2004).

[107] Y. Wang, R. Xu, W. He, Z. Yao, H. Li, J. Zhou, J. Tan, S. Yang, R. Zhan, G. Luo, and J. Wu, Three-dimensional histological structures of the human dermis, Tissue Eng., Part C **21**, 932 (2015).

[108] M. I. Porter and D. A. Hills, Note on the complete contact between a flat rigid punch and an elastic layer attached to a dissimilar substrate, Int. J. Mech. Sci. **44**, 509 (2002).

[109] T. D. Clemons, M. Bradshaw, P. Toshniwal, N. Chaudhari, A. W. Stevenson, J. Lynch, M. W. Fear, F. M. Wood, and K. S. Iyer, Coherency image analysis to quantify collagen architecture: Implications in scar assessment, RSC Adv. **8**, 9661 (2018).

[110] H. R. Hoogenkamp, G.-J. Bakker, L. Wolf, P. Suurs, B. Dunnewind, S. Barbut, P. Friedl, T. H. van Kuppevelt, and W. F. Daamen, Directing collagen fibers using counter-rotating cone extrusion, Acta Biomater. **12**, 113 (2015).

[111] N. Reznikov, R. Almany-Magal, R. Shahar, and S. Weiner, Three-dimensional imaging of collagen fibril organization in rat circumferential lamellar bone using a dual beam electron microscope reveals ordered and disordered sub-lamellar structures, Bone **52**, 676 (2013).